Numerical Investigation of the Effect of Cavity Flow on High Speed Train Pantograph Aerodynamic Noise

Hogun Kim[a,*], Zhiwei Hu[a], David Thompson[b]

[a]*Aerodynamics & Flight Mechanics Research Group, University of Southampton, Southampton, SO17 1BJ, United Kingdom*
[b]*ISVR Dynamics Group, University of Southampton, Southampton, SO17 1BJ, United Kingdom*

Abstract

Reducing train pantograph noise is particularly important. In this paper, the flow behaviour and noise contribution of simplified geometries representing high-speed train pantographs and the roof cavity at 1/10th scale are investigated. The Improved Delayed detached-Eddy Simulation (IDDES) turbulent model is used for the flow field simulation and the Ffowcs Williams & Hawkings aeroacoustic analogy is used for far-field noise prediction. The pantograph recess geometry is simplified to a rectangular cavity and two simplified DSA350 pantographs are included. The effect of the pantograph cavity is studied by comparing the flow behaviour and radiated noise from cases with and without the cavity, and also for different train running directions. When the pantographs are installed in a cavity, the shear layer, separated from the cavity leading edge, interacts with the pantographs, and generates large pressure fluctuations on the pantograph surfaces. In comparison with pantographs installed on a flat train roof, the flow around the pantographs with the cavity has different characteristics in terms of the velocity profile upstream of the pantographs. The study shows that the main noise source is from the panhead of the raised pantograph which produces strong tonal noise and this noise source is affected by the cavity flow.

Keywords: High-speed train, Aeroacoustics, Pantograph, Pantograph recess, Cavity flow, IDDES, Ffowcs Williams & Hawkings

1. Introduction

High-speed rail transportation has evolved into a thriving industry. Energy efficiency and environmental impact as well as journey time and price are the most important factors when competing with air and road transport. High-speed trains have a high capacity and are one of the most attractive forms of transport when travelling around 300 km/h [1].

However, train noise increases considerably as the speed increases; therefore, noise reduction has become an essential consideration in high-speed train design and is critical to the development, expansion, and operation of high-speed rail networks.

*Corresponding author
Email address: hk1g14@soton.ac.uk (Hogun Kim)

Below a certain speed, which is referred to as the transition speed, train noise is dominated by rolling noise, which is generated by the interaction between the wheels and rails [2], whereas aerodynamic noise becomes dominant above the transition speed [2, 3]. The transition speed depends on the train design, track condition and many other factors. Currently, aerodynamic noise becomes important above about 300 km/h. Aerodynamic noise from high-speed trains is believed to come mainly from the bogies, inter-coach gaps, the nose of the power car, the pantographs, and the pantograph recess [2, 3, 4, 5]. Baker reviewed the aerodynamic performance of high speed trains[6]. A number of researchers have focused on aerodynamic performance and flow features of the high speed train bogie and its cavity and their effect on the flow, such as the effect of different bogies geometries [7], its positions in leading and tail coach [8] and its different cavity geometries [9].

Noise from the bogies, the inter-coach gaps and the front nose can be shielded to some extent by conventional noise barriers; however, it is more difficult to shield the noise from the pantographs and their recess as they are located at the top of the train. A number of investigations on pantograph noise have been carried out in order to understand the noise source mechanisms and to find ways to reduce the radiated noise [10, 11, 12, 13, 14].

Grosche et al. [15] measured a full-scale DSA350 pantograph in a wind tunnel to obtain its noise source distribution. Three areas, the foot, the panhead and the knee connector, were identified as the main noise sources. Lölgen [16] carried out tests on full-scale DSA350SEK, ASP and PS206 pantographs in a wind tunnel at flow speeds ranging from 115 km/h to 400 km/h. Radiated noise spectra were analysed in detail; peaks at 550 Hz, 900 Hz and 3500 Hz in the noise spectrum of the DSA350SEK measured at 330 km/h were identified as being generated by the contact strip, the pantograph horn and the stroke limiting cage, respectively. Furthermore, there was no significant difference between the noise radiated from pantograph configurations with the joint either upstream or downstream.

Yu et al. [17] predicted the aerodynamic noise emission of a pantograph system at 350 km/h using a hybrid method of a non-linear acoustic solver (NLAS) and Ffowcs-Williams & Hawkings (FW-H) acoustic analogy. They found that the main noise source is the periodic vortex shedding, which generates Aeolian tones [3] around the pantograph structures, especially the panhead. Moreover, unsteadiness in the wake caused by flow separation downstream of the pantograph generates broadband noise. The computational study by Lei et al. [10] also indicated that the main pantograph noise sources were the vortices shed from its structures and that the strongest turbulent flows appeared around the panhead, knee joint and arm regions which generate mainly low and mid-frequency noise.

To predict the aerodynamic noise generated by a high-speed train pantograph, Latorre Iglesias et al. [18] introduced a semi-empirical

component-based model. The predictions from the model were compared with radiated noise measured for two different full-scale pantographs, giving good agreements for overall sound pressure level (OASPL), speed dependence and spectral shape.

Liu et al. [14] used the Delayed Detached Eddy Simulation (DDES) method to investigate the effects of the yaw angle of the pantograph arms. They found that by increasing the yaw angle of the cylindrical arm, the vortex shedding was reduced and aerodynamic force fluctuations were also decreased. These phenomena reduce the sound levels and the peak frequency.

Pantographs are usually located in a recess on the train roof, which houses the retracted pantograph and various electrical parts. Aerodynamic and acoustic features of the pantograph recess were investigated by Noger [19] using a 1/7 scale model of a TGV pantograph recess with two pantographs and an additional hood upstream. A baseline case of an empty recess was also investigated, which can be classified as a 'closed' cavity with a length-to-depth ratio of 11. It was found that most noise was generated in a region near the trailing edge of the cavity. When the pantographs were placed in the recess, the interactions between the wake of the pantograph and the downstream shear layer lowered the turbulence intensity at the downstream edge of the recess. On the other hand, as the upstream shear layer impinged on the pantograph surfaces, the turbulence intensity in the upstream region was increased. Furthermore, it was found that the shield located on the side of the roof reduced the shear layer and broadband noise. Noh et al. [5] assessed the aerodynamic noise induced by the recess of a full-scale Korean high-speed train (KTX) experimentally. The noise from the recess was found to be mostly below 1200 Hz and at a similar level to that from the pantograph itself at a speed of 300 km/h.

The boundary layer thickness on the train roof may affect the radiated noise from the cavity and the pantographs. Carnevale et al. [20] investigated the effect of the lift and drag forces on the mean contact force acting between a pantograph and the contact wire using a shear stress transport (SST) $k-\omega$ Reynolds-averaged NavierStokes (RANS) model. When the pantograph and the recess were placed on a middle coach, the incoming flow of the upper arm and the panhead region of the pantograph is about 20% slower than the speed for a case with a very thin boundary layer.

Jia et al. [21] carried out a numerical investigation of the boundary layer and wake flow features with three different train lengths at 1/8 scale at a speed of 60 m/s. They found that the boundary layer became thicker along the train length, and there was a significant difference between the boundary layer thickness of the leading coach and the tail coach.

Several researchers have investigated noise reduction techniques for pantographs. Ikeda et al. [11] optimized the shape of the panhead and tests were carried out in a wind tunnel. Holes were made through the panhead along the span in order to decrease the intensity of the Aeolian tone. The optimized panhead significantly reduced the noise for an isolated panhead. However, they found that the optimised shape did not effectively reduce the noise when it was installed on the articulated frame. The reason was that strong

aerodynamic interference occurred between the optimised panhead and the articulated frame. Ikeda and Mitsumoji [12, 13] explained the details of this interference through computational simulations and they found a distinct vortex which occurred from the panhead support towards the panhead. To prevent the aerodynamic interference, a new panhead support was developed which generates less vortical structures around the joint between the panhead and its support. The design generated an OASPL approximately 4 dB less noise than the baseline case.

However, much less attention has been given to the generation of aerodynamic noise from the pantograph recess and its reduction. Moreover, interactions of the recess with pantograph components are less well understood. Therefore, this paper aims to provide improved understanding of aerodynamic phenomena and noise generation mechanisms from cavity flow and its effect on the pantograph, using computational methods. The Improved Delayed Detached-Eddy Simulation (IDDES) approach is used to resolve details of the turbulent structures and enable sufficiently accurate noise prediction. For an example configuration of one raised and one retracted pantograph cases with and without cavity are compared.

The paper is structured as follows: in Section 2, the methodologies employed are introduced including the turbulence model and acoustic analogies. Section 3 describes the computational set-up and a benchmark case is used to demonstrate the applicability of the numerical method. Section 4 describes the geometry and the mesh set-up used for this study. Section 5 presents the computational aerodynamics results, while aeroacoustic results are presented in section 6. Finally, conclusions are summarised in Section 7.

2. Methodology

For the typical operational speed of modern high-speed trains, the Mach number is generally less than 0.3, which allows the flow to be treated as incompressible [22]. Therefore, the unsteady incompressible Navier-Stokes (N-S) equations are solved for flow over pantographs. These are given in tensor notation as,

$$\frac{\partial u_j}{\partial x_j} = 0 \tag{1}$$

$$\frac{\partial u_i}{\partial t} + u_j \frac{\partial u_i}{\partial x_j} = -\frac{1}{\rho}\frac{\partial p}{\partial x_i} + \nu \frac{\partial^2 u_i}{\partial x_j \partial x_j} \tag{2}$$

where ρ is the density of the fluid, t is time and u_i is the flow velocity in the x_i direction with $i = 1, 2, 3$ representing the streamwise, cross flow and spanwise directions, respectively. p is the pressure, and ν is the kinematic viscosity.

2.1. Improved Delayed Detached-Eddy Simulation

In order to achieve reasonably high accuracy while avoiding excessive computational cost, Detached Eddy Simulation (DES) can be considered for numerical solutions of practical applications with complex geometries. DES is a hybrid method combining unsteady Reynolds-Averaged Navier-Stokes (URANS) and Large-Eddy Simulation (LES) methods [23]. This hybrid modelling approach combines the benefits of RANS and LES while minimising their disadvantages. In near-wall regions, URANS with the Spalart-Allmaras (S-A) model is used to represent the flow, which is useful to relax the strong LES mesh constraints close to solid surfaces. Meanwhile LES with a single-equation model for the Subgrid-scale (SGS) viscosity is used in separated flow regions dominated by large turbulence scales. However it is important to provide a sufficient number of grid points with a moderate expansion ratio in the direction normal to the wall to resolve the boundary layer [24].

The DES method combines RANS and LES by replacing the length scale based on mesh information and wall distances in the transport equation and using the RANS model for modified eddy viscosity [23]. However, this method has some limitations within the attached boundary layer. In the case of an ambiguous mesh with high aspect ratios in the boundary layer, the grids may be fine enough in the wall-normal direction to activate the DES limiter to switch to the LES mode, but not fine enough to support resolved fluctuating velocities within the boundary layer. This can induce early separation, called grid-induced separation [25]. The DES method was improved to address this issue leading to the Delayed DES (DDES) method [25]. Later it was found that DDES may cause logarithmic-layer mismatch [27]. Shur [27] introduced Improved DDES (IDDES) in order to solve this problem by using a new subgrid length-scale, related to the grid spacing and the wall distance. This model for unsteady inlet conditions allows the Wall-Modeled LES (WMLES) mode to be activated within the boundary layers. The IDDES model is used in the current work by using the software, STAR-CCM+.

2.2. Ffowcs Williams & Hawkings acoustic analogy

The FW-H equation is an exact re-arrangement of the N-S equations, to give a wave operator on the left-hand side and all other terms on the right-hand side to represent equivalent noise sources [28, 29, 30]. The FW-H analogy consists of two surface source terms, the thickness (monopole) and loading (dipole) terms, and a volume source term, representing the quadrupole sources. The quadrupole term is neglected in this study because its contribution is insignificant for low Mach number flow compared with the other two sources. This assumption has been used successfully for low Mach number flow noise predictions for high-lift devices [31, 32], aircraft landing gear [33, 34], and high-speed train noise prediction [35, 36]. The FW-H equation is solved to obtain the far-field acoustic pressure by using the aerodynamic near-field data as input.

Brentner and Farassat [37, 38] developed the following time domain solution for the FW-H equations to predict noise for subsonic flow, known as Formulation 1A:

$$p'(\mathbf{x},t) = p'_T(\mathbf{x},t) + p'_L(\mathbf{x},t) \tag{3}$$

where $p'_T(\mathbf{x},t)$ and $p'_L(\mathbf{x},t)$ are the thickness and loading noise contributions respectively.

In this study, as the integration surfaces are taken as the solid surfaces, $p'_T(\mathbf{x},t) = 0$ and only loading noise contributions are considered, given by:

$$\begin{aligned} p'_L(x,t) = \frac{1}{4\pi}\Bigg(\frac{1}{c_0}\int\left[\frac{\dot{L}_r}{r(1-M_r)^2}\right]_{ret} dS + \int\left[\frac{L_r - L_M}{r(1-M_r)^2}\right]_{ret} dS \\ + \frac{1}{c_0}\int\left[\frac{L_r(r\dot{M}_r + c_0 M_r - c_0 M^2)}{r^2(1-M_r)^3}\right]_{ret} dS\Bigg) \end{aligned} \tag{4}$$

with

$$L_i = P_{ij}n_j + \rho u_i(u_n - v_n) \tag{5}$$

and

$$P_{ij} = (p - p_0)\delta_{ij} - \sigma_{ij} \tag{6}$$

where M_i is the Mach number in the x_i direction and M_r is the Mach number in the observer direction, the bracket $[\,]_{ret}$ denotes that the quantities are evaluated at retarded time $\tau = t - |x-y|/c_0$, c_0 is the speed of sound, r is the distance from a source point to the observer, u_n is the fluid velocity component normal to the surface, v_n is the surface velocity component normal to the surface, P_{ij} is the compressive stress tensor, σ_{ij} is the viscous stress tensor, and p_0 is ambient pressure.

For the far-field noise prediction in this study, the solid surface term of the FW-H method based on Farassat's formulation 1A is used for all numerical cases.

3. Validation of the methodology

3.1. Cavity near-field validation

The numerical procedure used is validated first for a clean cavity against experiments of Plentovich et al. [39], who investigated the effect of the cavity length-to-depth ratio L/D on the cavity wall pressure distribution at subsonic and transonic speeds. In this paper, simulations are carried out for a cavity with L/D = 12 at a Mach number M = 0.2, and compared with the experimental data [39].

3.1.1. Geometry and flow conditions

A planar cavity is investigated, which comprises a simple rectangular cutout in an otherwise infinite plate and can therefore be described by its length-to-depth (L/D) and width-to-depth (W/D) ratios. The cavity considered has a length L = 0.731 m and a depth D = 0.061 m, giving L/D = 12, and a width W = 0.243 m, giving W/D = 4, as shown in Figure 1. The computational domain extends $36D$ downstream of the cavity, $16D$ vertically and $8D$ laterally from the cavity edge to each side. An upstream length of about $12D$ was determined (and checked after the simulation was run) so that the computed boundary layer upstream of the cavity has approximately the same thickness (δ = 0.011 m) as in the experiment (δ = 0.0125 m) [39].

For the boundary conditions of the simulations, no-slip conditions are defined on all walls of the cavity and the floor; the two side and top boundaries of the domain are defined as symmetric boundaries. An outflow boundary with zero gauge pressure was used at the downstream boundary. A velocity inlet is specified at the inflow with a freestream Mach number of 0.2 (speed 70.2 m/s) corresponding to a Reynolds number of 2.2×10^6 based on the cavity length.

In the present study, a Hexa-dominant mesh was generated using the internal automatic mesh generator of the commercial software STAR-CCM+ (called trimmed mesh in STAR-CCM+). For the purpose of the mesh independence study, four meshes were generated with different mesh densities. The strategy used in the mesh independence study is that Δy, the first cell height from the wall, is kept constant whereas Δx and Δz, the cell lengths in the x-direction and the z-direction respectively, are refined. The maximum ratios of $(\Delta x, \Delta z)_{max}$ / Δy are given in Table 1 for each refinement zones and criteria for each zone and Table 2 for each along with the total number of cells.

Table 1: The refinement zones and mesh criteria for each zone.

$(\Delta x, \Delta z)_{\max}/\Delta y$	Refinement region	Number of zones	Min. cell size (mm)
120	Cavity leading edge	1	0.8
	Cavity trailing edge	2	0.8
	Cavity inside	1	0.8
	Cavity side edge	2	1.5
	Cavity overall	2	8
200	Cavity leading edge	1	1.2
	Cavity trailing edge	2	1.2
	Cavity inside	2	1.2
	Cavity side edge	2	2.5
	Cavity overall	2	9
400	Cavity leading edge	1	2.5
	Cavity trailing edge	2	2.5
	Cavity inside	2	2.5
	Cavity side edge	2	4
	Cavity overall	2	9
670	Cavity leading edge	1	4
	Cavity trailing edge	2	4
	Cavity inside	2	4
	Cavity side edge	2	4
	Cavity overall	2	9

Table 2: Mesh criteria for each cases for the cavity model.

	Coarse			Fine
$(\Delta x, \Delta z)_{\max}/\Delta y$	670	400	200	120
Total number of cells	4 million	6 million	26 million	30 million

Seven refinement blocks are used to generate the meshes with improved resolution in areas with strong flow variations. The refinement zones are indicated in Figure 2. As intensive turbulent and vortical flow occurs in the cavity region and at the cavity trailing edge, refined resolutions are used with a surface growth rate of 1.1 and a boundary layer stretching ratio of 1.12.

As the Spalart-Allmaras (S-A) turbulence model is used in the near-wall region, it was ensured that y_1^+ values are limited to less than 1 along all solid walls [26]; y_1^+ is the non-dimensional wall distance of the first off-wall grid points ($y_1^+ \equiv \frac{u_* y}{\nu}$, where u_* is the friction velocity, y_1 is the distance of the first grid point to the wall, and ν is the kinematic viscosity). The maximum Courant-Friedrichs-Lewy (CFL) number is set to 1 for simulation stability. A second-order implicit scheme is applied for time marching. For the convection term, a combination of the second-order upwind and bounded central-differencing convection scheme is used.

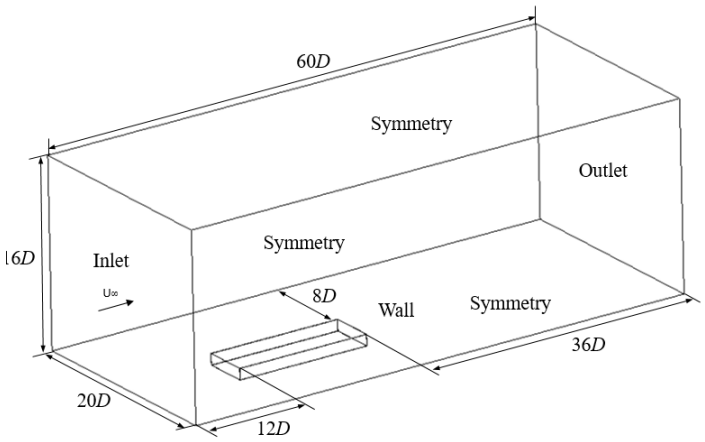

Figure 1: Computational domain and boundary conditions for validation study [39] (not to scale).

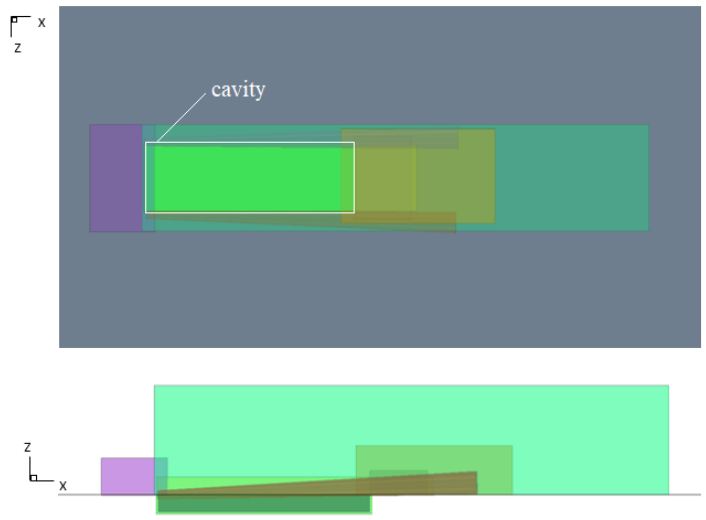

(a)

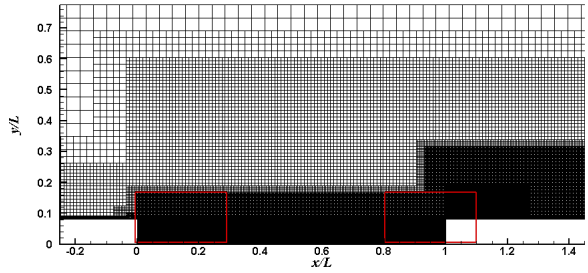

(b)

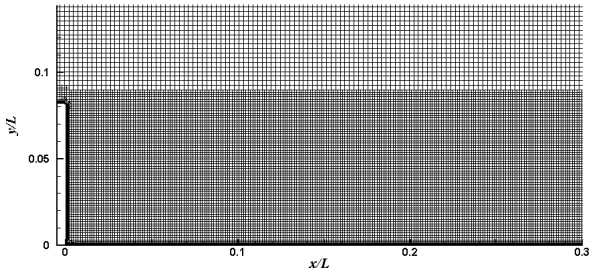

(c)

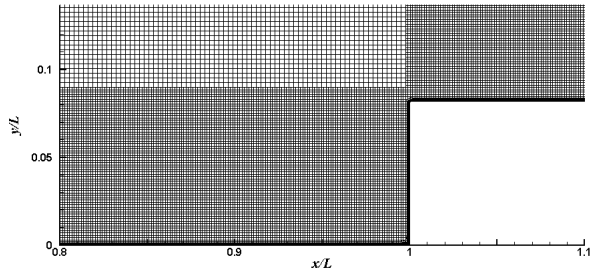

(d)

Figure 2: Mesh refinement zones (a), overall mesh (b), detail view of leading mesh (c) and trailing meshes of aspect ratio 120 (fine) for the cavity model.

3.1.2. Validation of the numerical results

The mean surface pressure coefficients on the cavity floor ($C_p = \frac{p-p_\infty}{\frac{1}{2}\rho_\infty U_\infty^2}$, where p is the surface pressure and p_∞ is the static pressure in the freestream) calculated using the four meshes are compared with the experiment [39] in Figure 3. As the mesh is refined (Δx / Δy, Δz / Δy become smaller), the pressure distribution converges. The distributions from the meshes with maximum

cell aspect ratios 200 and 120 are in good agreement with the experimental data. Considering the balance between the accuracy of the result and the computational cost, the set-up based on the ratio 200 is chosen as the basis for generating meshes for the other cases in the paper.

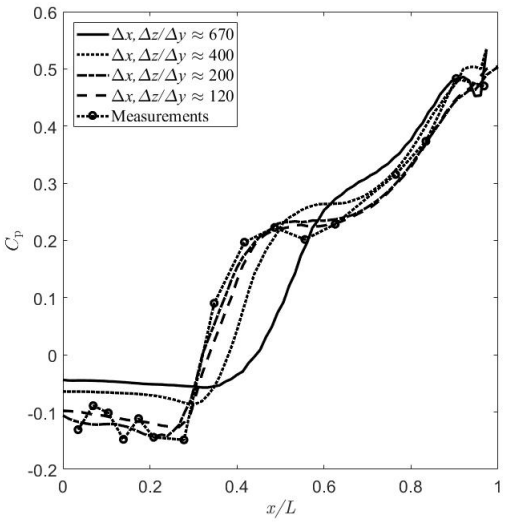

Figure 3: Comparison of the cavity floor pressure distributions at Mach number 0.2 for computational results using different meshes and experimental data [39].

4. Computational set-up

4.1. Geometry

The geometry is chosen to represent a simplified 1/10 scale high-speed train pantograph roof cavity of a TGV train with two DSA 350 pantographs (one raised and one retracted). Owing to the complexity of the actual pantograph, it is necessary to simplify its geometry to reduce the computational resource requirements. The pantograph cavity is simplified to a rectangular cavity with dimensions L = 0.812 m, D = 0.07 m and W = 0.29 m, giving L/D = 11.5, W/D = 4.1. Most of the parts of the pantograph are retained, apart from small components such as straps, springs and wire arms. Table 3 gives a list of the retained and omitted parts of the pantograph. The pantograph model is shown in Figure 4.

Since this study investigates the effect of the cavity on the flow, cases with the pantographs installed directly on top of the train roof without the cavity are also studied (cases 3 and 4). An empty cavity (without pantographs in the cavity) is also considered for comparison (case 0). To consider effects of the train running direction, the freestream direction is set as the positive x-direction for cases 1 and 3, and the negative x-direction for cases 2 and 4, as shown in Figure 4 (a).

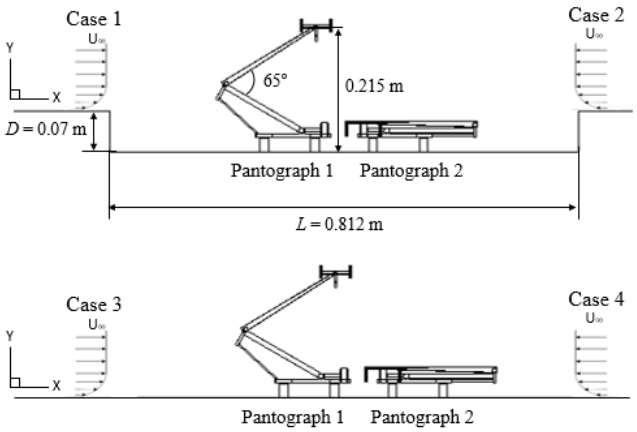

(a) Side view

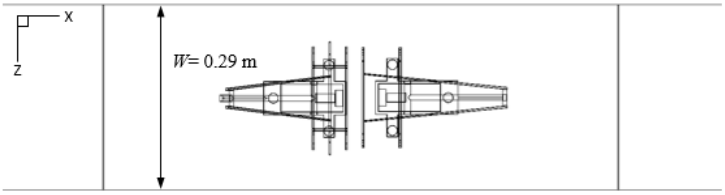

(b) Top view

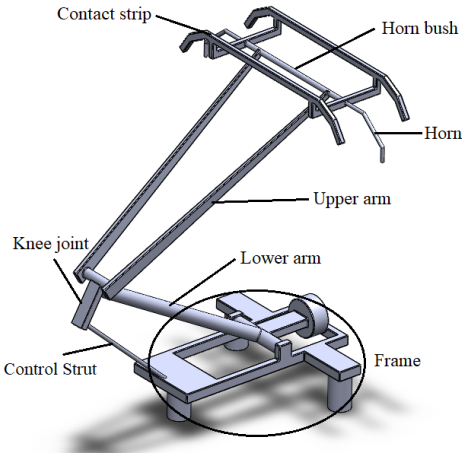

(c) Overview of the raised pantograph

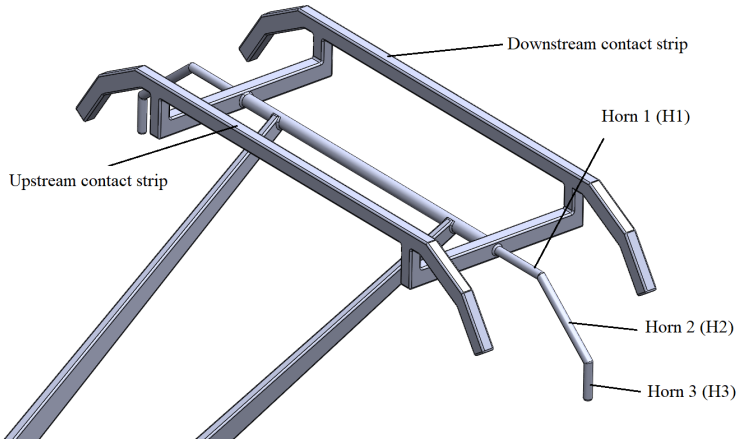

(d) Detail of the panhead

Figure 4: Description of the geometry

Table 3: List of retained and omitted parts

Regions	Retained parts	Omitted parts
Panhead	Contact strip, horn bush, horn	Straps, head lowering, spring,
Upper arm	Upper arm, knee joint	Guide head, wire arms
Lower arm	Lower arm, control strut	

4.2. Numerical test section

The computational domain, as illustrated in Figure 5, extends over $56D$, $29D$ and $4.1D$ along the streamwise (x), vertical (y) and spanwise (z) directions, respectively. The upstream length was determined as $30D$ in order to have a fully-developed turbulent boundary layer at the cavity leading edge for all cases. The cavity and pantograph walls are defined as no-slip walls. The outlet and top boundaries are sufficiently far away to have negligible effect on the flow developed around the cavity. The top boundary is specified to have symmetry conditions and a pressure outlet is imposed at the outlet boundary. Periodic boundary conditions are applied to the two side surfaces of the domain. The inflow boundary is set as a velocity inlet with incoming flow velocity $U_\infty = 83.3$ m/s (300 km/h), corresponding to a Reynolds number of 3.89×10^5 (based on the freestream properties and the cavity depth).

For all cases in this study, a Hexa-dominated mesh (called trimmed mesh in STARCCM+) is used and these meshes are generated using the STAR-CCM+ mesh generator with refinement zones. Different cell sizes are specified for each refinement zone; an example is shown in Figure 6. As high gradients of pressure and velocity occur in the vicinity of the cavity trailing edge and the pantographs, these regions are refined with a minimum cell size of 1.2 mm in the cavity trailing edge region and 0.4 mm in the pantograph panhead region, and a surface growth rate of 1.1. The maximum cell aspect ratio is 200 (Δx / Δy, Δz / $\Delta y = 200$) as discussed in section 3. In order to reduce the computational costs while retaining a sufficient accuracy, the boundary layer mesher (also called prism layer mesher in STAR-CCM+) is used. 25 - 40 layers are used in order to resolve the boundary layer region. The mesh topology and details of the mesh around the panhead are shown in Figure 6. The total number of cells for each case is listed in Table 4. It is verified that y_1^+ is less than 1 on all surfaces. In order to ensure a stable simulation, a non-dimensional time step $U\Delta t/D$ = 0.0095 is used, where D is depth of cavity, which ensures that the CFL number is less than 1 for all cases.

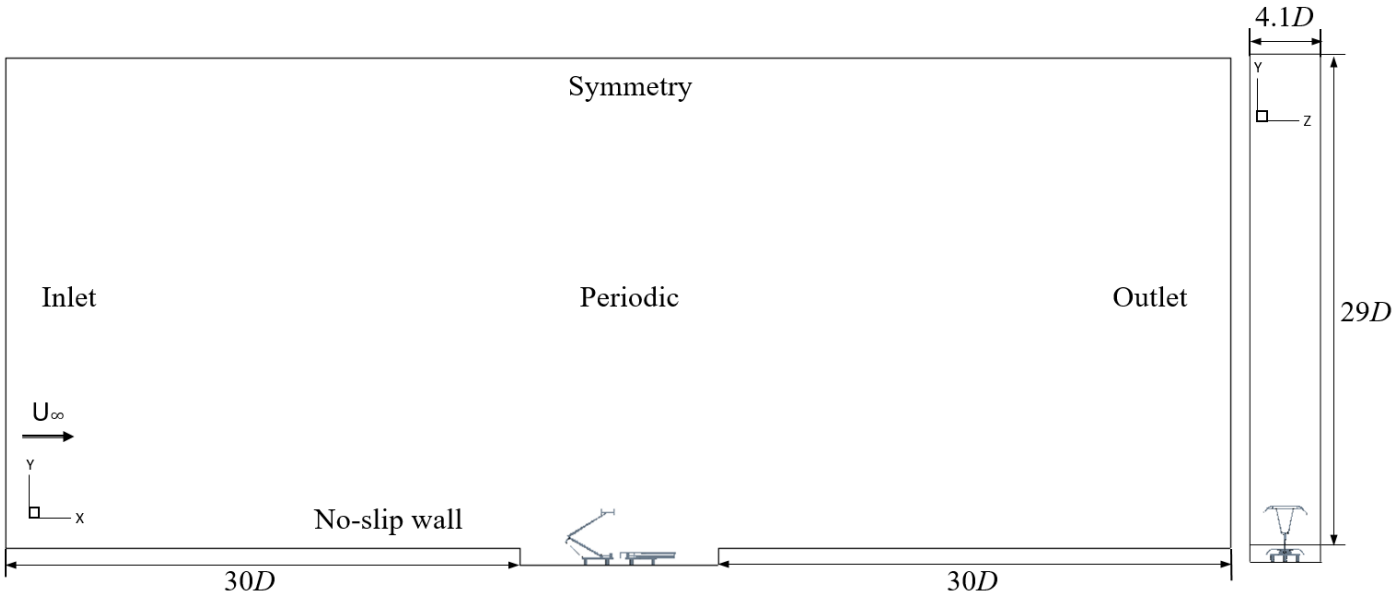

Figure 5: Computational domain and boundary conditions

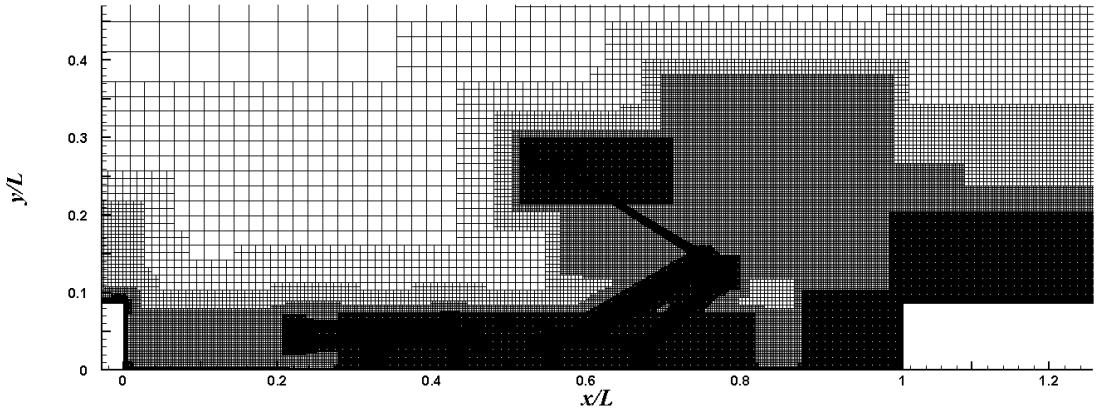

(a) Overall view of the mesh

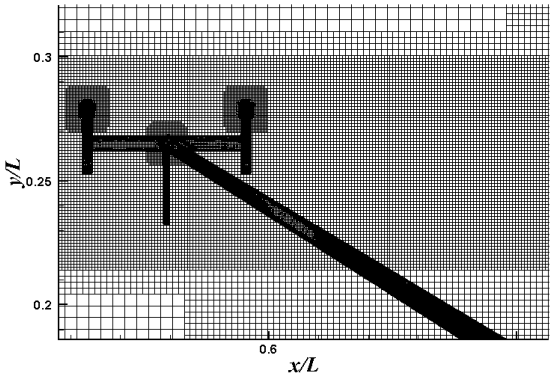

(b) Details view of the mesh

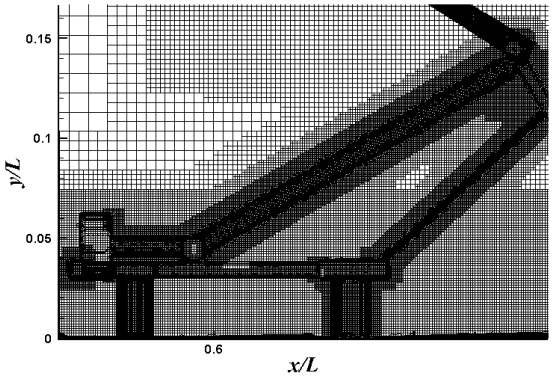

(c) Details view of the panhead mesh

Figure 6: Overview and detail of the meshes

Table 4: Summary of the cases considered

Simulation cases	Description of the case	Number of cells
Case 0	Empty cavity	14.8 million
Case 1	Front pantograph raised with the cavity	30.4 million
Case 2	Rear pantograph raised with the cavity	29.4 million
Case 3	Front pantograph raised without the cavity	27.8 million
Case 4	Rear pantograph raised without the cavity	25.7 million

5. Aerodynamic results

In order to investigate the near-field flow characteristics and potential acoustic sources of the cavity and pantographs, the time-averaged velocity, wall pressure fluctuations and instantaneous flow fields are analysed and compared for the cavity without and with

pantographs.

5.1. Q-criterion

To provide an overview of the flow field and analyse its interaction with the pantographs, three-dimensional vortical structures are illustrated in Figure 7, based on the Q-criterion. Q is the second invariant of the velocity gradient, can be written as: $Q = \frac{1}{2}(\Omega_{ij}\Omega_{ij} - S_{ij}S_{ij})$, where Ω_{ij} is the vorticity tensor and S_{ij} is the rate-of-strain tensor. These can be defined as $\Omega_{ij} = \frac{1}{2}\left(\frac{\partial u_i}{\partial x_j} - \frac{\partial u_j}{\partial x_i}\right)$, $S_{ij} = \frac{1}{2}\left(\frac{\partial u_i}{\partial x_j} + \frac{\partial u_j}{\partial x_i}\right)$. $Q_{\mathrm{norm}} = \frac{QD^2}{U_\infty^2}$ is the normalized value of Q, where D is the cavity depth, and U_∞ is the freestream velocity. Q shows the local balance between vorticity and shear strain rate magnitude. Regions of positive Q indicate the vortical flow dominates.

The iso-surface of the normalized Q-criterion is plotted for Q_{norm} = 2.5 in Figure 7 and is coloured by the non-dimensional instantaneous velocity magnitude. In general, vortices are generated in the wakes of pantograph components, especially the panhead, the upper and lower arms, and also in front of the pantographs. When the pantographs are placed in the cavity (cases 1 and 2), the shear layer, due to the flow separation from the cavity leading edge, rolls up and generates spanwise vortical structures in a recirculation region between the upstream wall of the cavity and the front pantograph and these vortical structures evolve and become hairpin vortices as they are convected downstream of the reattachment of the shear layer. This detail of coherent vortical structures can be seen in Figure 8. Spanwise vortical structure in case 2 is dissipated earlier than in case 1 due to presence of the folded pantograph in the upstream of the cavity. Hairpin vortical structures are seen in most of the upstream region of the cavity in case 2. In case 1, however, the vortical structure is dissipated after interacting with the raised pantograph. In case 2, stronger unsteady flow is observed in the region downstream of the cavity than in case 1. This is due to flow interactions between the raised pantograph and the cavity downstream wall. Furthermore, highly unsteady flows occur in the cavity downstream region, as shown in Figure 7 (a) and (b). The trailing edge generates flow separation and highly unsteady flow. The streamwise vortical structures from the trailing edge separated flow rapidly develop into hairpin vortical structures, which will lead to high pressure fluctuation on cavity trailing edge walls.

For cases 3 and 4, without the cavity, a highly unsteady flow is seen behind the panhead of the raised pantograph and the frame of both pantographs. The vortices from the upstream contact strip roll up and rapidly develop into hairpin vortices, similar to those in cases 1 and 2. For case 4, the joint of the folded pantograph and the upper arms of the raised pantograph generate higher unsteady flow with stronger vortical structures than in case 3, as shown in Figure 7 (d). Furthermore, most of the vortical structures become streamwise vortices in the downstream region. Compared with the cases with the cavity, strong vortices are generated by the frame of the raised pantograph and the whole folded pantograph in the cases without the cavity. These vortices strongly interact with the

rear pantograph components.

These results suggest that the cavity (in cases 1 and 2), folded pantograph and the frame of the raised pantograph (in cases 3 and 4) and the panhead of the raised pantograph in all cases produce a highly unsteady flow.

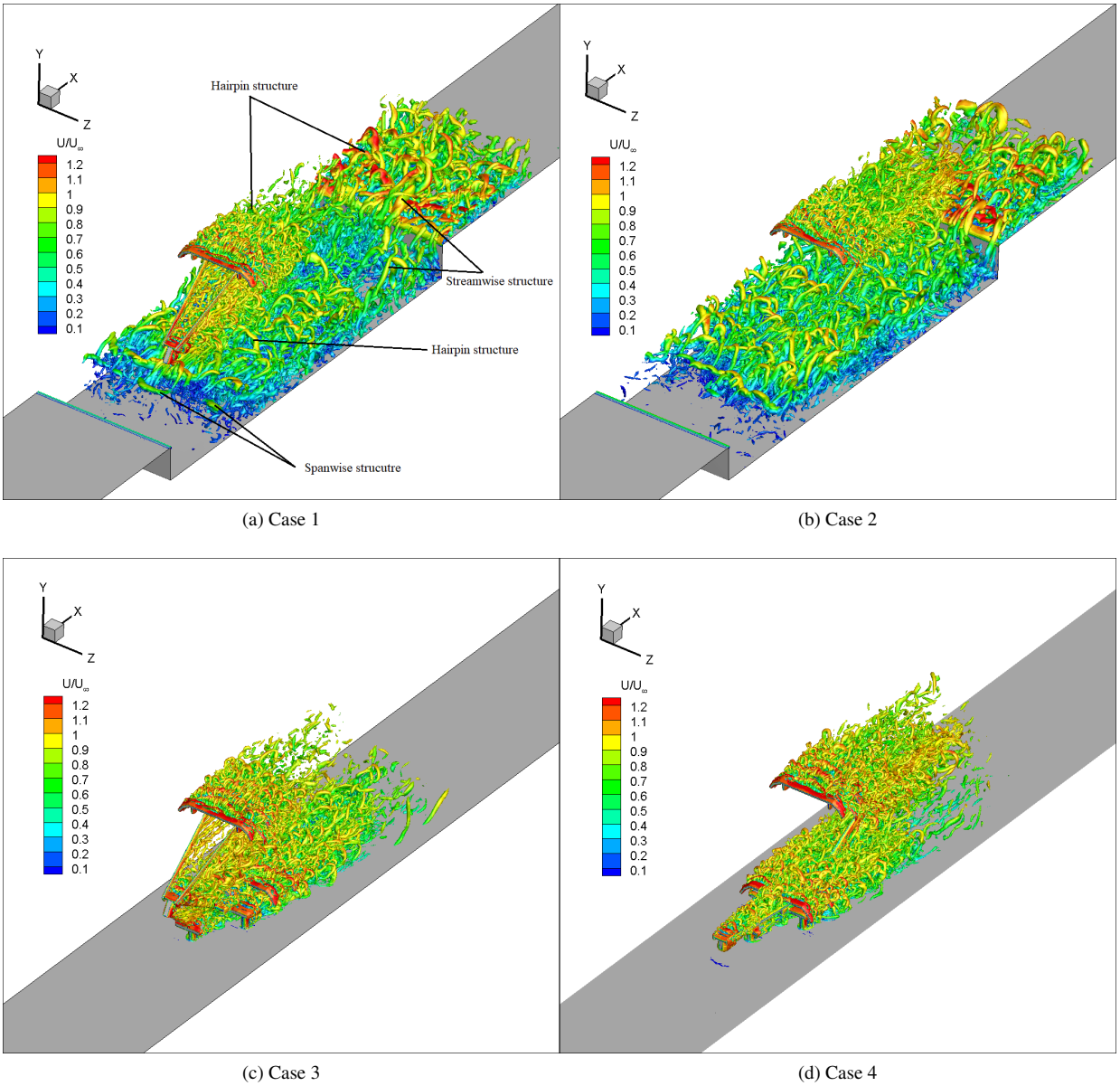

(a) Case 1

(b) Case 2

(c) Case 3

(d) Case 4

Figure 7: Flow structure demonstrated by iso-surface of Q-criterion Q_{norm}=2.5

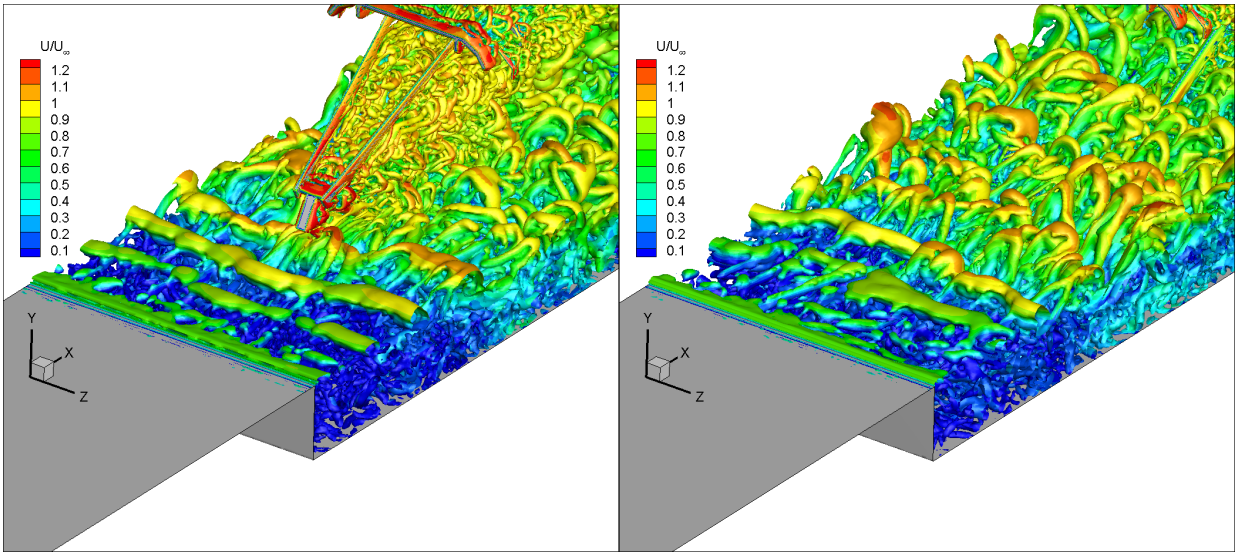

(a) Case 1 (b) Case 2

Figure 8: Flow structure in the shear layer region by iso-surface of Q-criterion Q_{norm}=0.14

5.2. Time-averaged velocity field

Figure 9 displays contours of the mean streamwise velocity with two-dimensional in-plane streamlines at the mid-span plane ($z = 0.145$ m). In this paper, it is assumed that the pantographs and the recess are placed on the top of the leading coach. However, some high speed train has them in the middle of the coach. Therefore, it is noted that the boundary layer in front of the cavity could be thicker than for the cases in this paper [20, 21]. This means that incoming flow speed in the vicinity of the rasied pantograph is slower than that in the cases in this paper (12% in the panhead region [20]).

For the two cases in which the pantographs are located inside the cavity (cases 1 and 2), the incoming flow boundary layer separates from the cavity leading edge, the shear layer from this separated flow impinges around the middle of the cavity floor and the flow reattaches at $x/L = 0.6$. The cavity has a length-to-depth ratio $L/D = 11.5$ which is a classic closed cavity, as confirmed by the simulation shown in Figure 9 (a). The shear layer impinges on the cavity floor and the pantographs in both cases 1 and 2. In case 1 (raised pantograph in front), the shear layer impinges on the front foot, frame and control strut of the raised pantograph, whereas for case 2 impingement of the shear layer occurs on the panhead region of the folded pantograph. This impingement may generate surface pressure fluctuations, which would produce noise.

In the region upstream of the cavity, the mean flow behaviours of the three cavity cases (cases 0, 1 and 2) are similar. In both cases, flow separation at the cavity leading edge introduces a recirculation region between the cavity leading edge and the front pantograph.

This similar separated flow and the recirculation also were indicated by Noger [19]. However, presence of 'U' shaped hood in the work by Noger [19], the separated flow impinged on the cavity floor earlier than case 1 and 2. Case 2, as shown in Figure 9 (c), has a smaller recirculation region than case 1 due to turbulent flow interaction with the front folded pantograph. For both cases 1 and 2, a small recirculation region appears at the upstream bottom edge and another small recirculation region can be observed in the gap between the two pantographs. Furthermore, another recirculation is found at the downstream bottom corner in all cavity cases (cases 0, 1 and 2). The shape and size of this separation region is altered by the installed pantographs. Flow separates again at the trailing edge and reattaches on the cavity aft wall further downstream at $x/L = 1.10$ for case 1, and at $x/L = 1.15$ for case 2. The flow recirculation region at the aft wall is influenced by turbulent flow generated by the pantographs. The flow direction in the vicinity of the cavity trailing edge for case 1 (Figure 9 (b)) is more upward than for case 2. This is due to the wake from the raised pantograph. When the knee is upstream in case 1 (raised pantograph in front) this generates a larger wake region than with the knee downstream in case 2.

Highly unsteady flow occurs in the vicinity of the cavity with low velocity in cases 1 and 2. The direction of the streamlines passing through the panhead of the raised pantograph is slightly more downward, which is associated with the cavity flow. Moreover, the incoming flow velocity in the vicinity of the panhead in cases 1 and 2 is slightly lower than for the cases without cavity, which will be analysed in more detail later. The wake region around the panhead for cases 3 and 4 is slightly larger than that for cases 1 and 2. In cases 3 and 4, small recirculation regions are found at the back of the feet, joint and frame of the pantographs, which are similar to those found for cases 1 and 2. Furthermore, for cases 3 and 4, a large wake region is generated by the rear pantograph frame.

As the recess is simplified, the insulators in the recess are omitted. When insulators are present in the recess area, flow inside the cavity will interact with the insulators. The velocity profile would be slightly changed inside the cavity due to the presence of the insulators. However, the shear layer impingement location and the separated flow from the trailing edge would not be affected by the insulators significantly as the insulators are located inside the cavity where the flow speed is generally low.

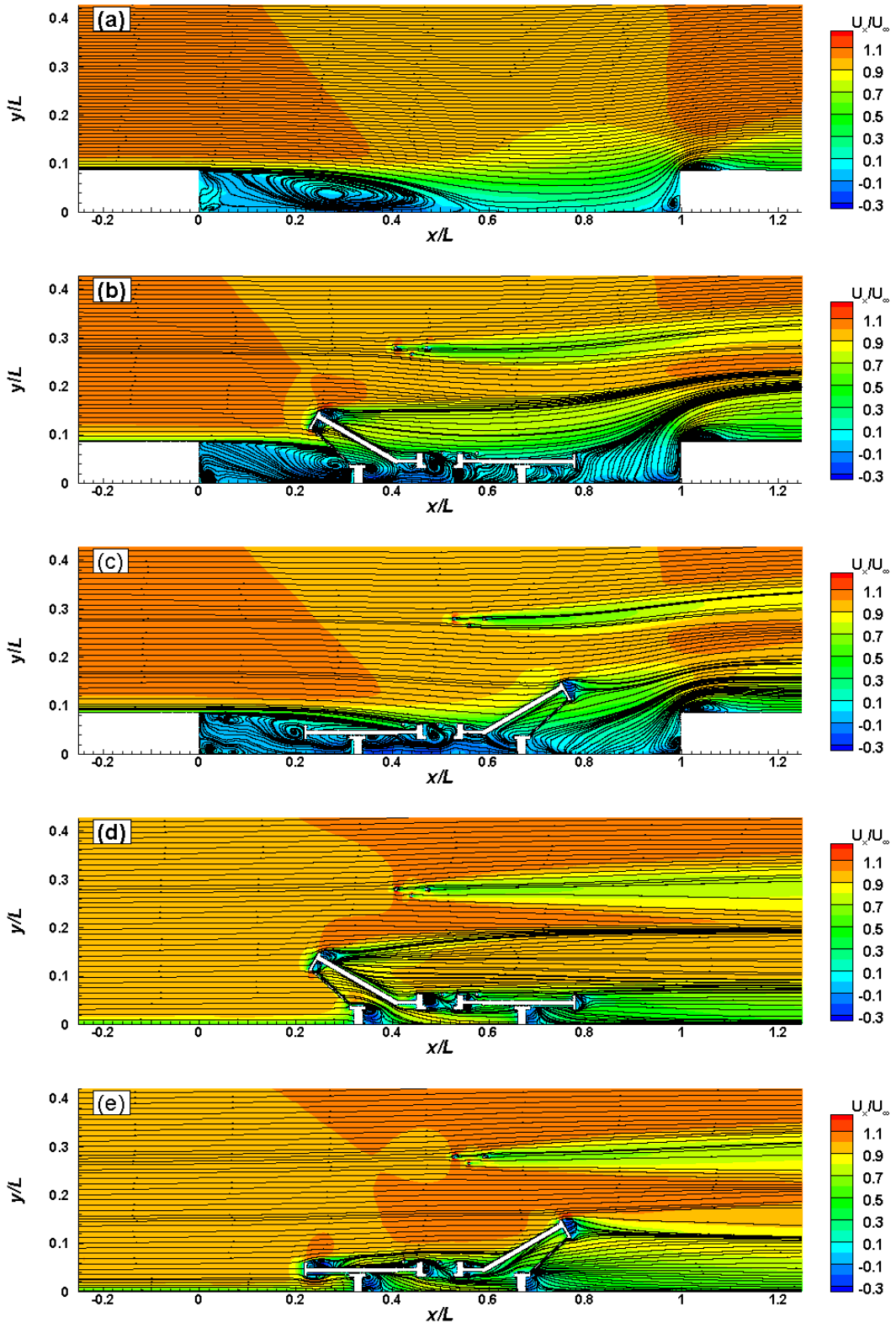

Figure 9: Mean streamlines with time-averaged velocity contours, (a) case 0 (empty cavity), (b) case 1, (c) case 2, (d) case 3, (e) case 4.

As the panhead of the raised pantograph is a major source of noise [16], the flow velocity ahead of the panhead is an important factor influencing the radiated noise. In order to investigate the development of the flow and the mean streamwise velocity U_x from the cavity leading edge to the panhead of the raised pantograph, the development of velocity for the empty cavity is investigated first. This is shown in Figure 10, which gives the profiles of U_x at different streamwise locations. A typical boundary layer profile is seen upstream of the cavity until flow separates at the leading edge (x = 0). Due to the recirculation zone formed at the front part of the cavity, here negative velocity is seen near the cavity bottom. It is also observed that U_x outside the cavity decreases slightly downstream and the lowest velocity appears at $x/L = 0.451$. The streamwise velocity at a height of $y = 3D$, which is at a similar height to the panhead location, reduces by up to approximately 4% (from $1.01U_\infty$ to $0.97U_\infty$) away from the cavity leading edge. This occurs because the fully developed turbulent flow at $x/L = 0$ enlarges into the expanded area. This expanded area affects the flow velocity outside the cavity. This is important for the noise generation as the flow speed has a strong influence on the noise generated.

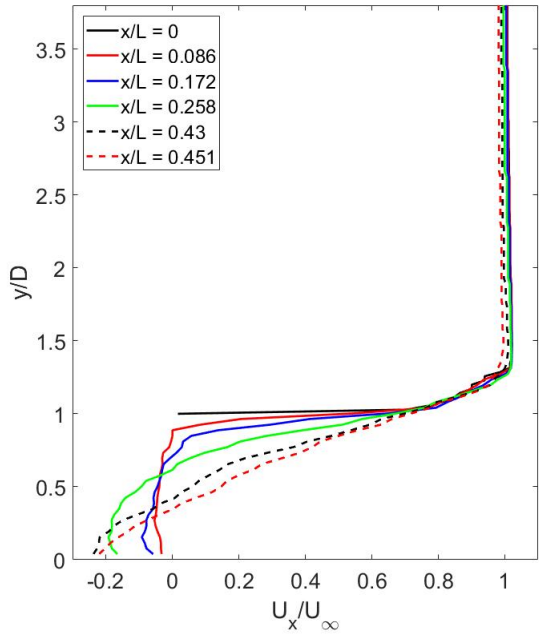

Figure 10: Time-averaged x-velocity on vertical lines at $z = 0.5W$ for empty cavity.

Figures 11 and 12 display the profiles of U_x at different streamwise and spanwise locations for the four cases with pantographs. The lines at $x/L = 0.43$ for cases 1 and 3 are located just before the upstream contact strip of the raised pantograph and the lines at $x/L = 0.45$ are just in front of the horn of pantograph. In cases 2 and 4, the lines at $x/L = 0.52$ and at $x/L = 0.54$ are located at

the upstream contact strip and the horn of the raised pantograph.

The profiles in cases 1 and 2 are similar upstream of the pantographs ($x/L = 0 \sim 0.26$) within the cavity ($y/D = 0 \sim 1$); negative values of the streamwise velocity U_x start to appear after the cavity leading edge between $y/D = 0$ and 1 due to the cavity recirculation. In general, the flow speed in the cavity region is smaller than the corresponding cases without the cavity. This means that although the cavity causes unsteady flow around the cavity, it reduces the flow speed at the folded pantographs and lower parts of the raised pantograph. This shielding effect by the cavity was also indicated by Carnevale et al. [20]. The slightly lower flow speed, seen in Figure 10, is also observed outside the cavity region in cases 1 and 2 away from the leading edge of the cavity. At $x/L = 0.43$ (before the panhead of the raised pantograph) and $x/L = 0.45$ (before the horn of the raised pantograph), the values of U_x between $y/D = 3$ and 3.5 in case 1 are about 5% lower than in case 3 due to the cavity flow. A similar tendency can be seen at $x/L = 0.52$ and 0.54 in cases 2 and 4 as shown in Figure 12 (g) and (h).

The influence of the cavity on the flow upstream of the panhead suggests that the noise from the upper part of the raised pantograph (including panhead and upper arms) will be different between the cases with the cavity (cases 1 and 2) and the cases without (cases 3 and 4). This will be discussed in more detail in the aeroacoustic results section.

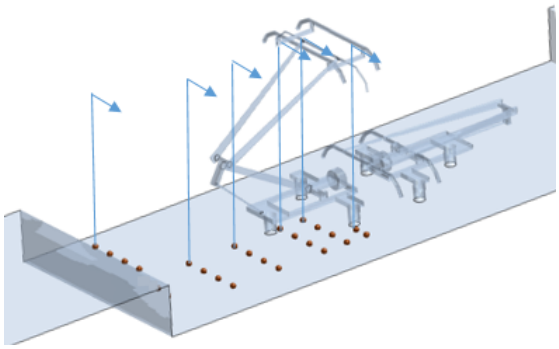

(a) Line positions

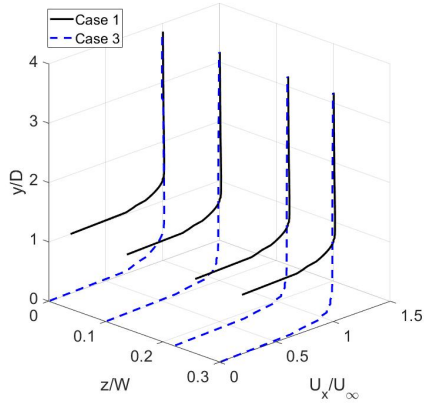

(b) $x/L = 0$

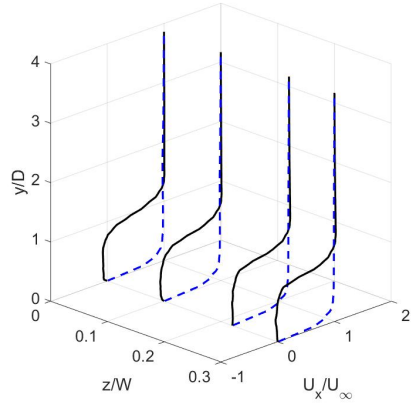

(c) $x/L = 0.17$

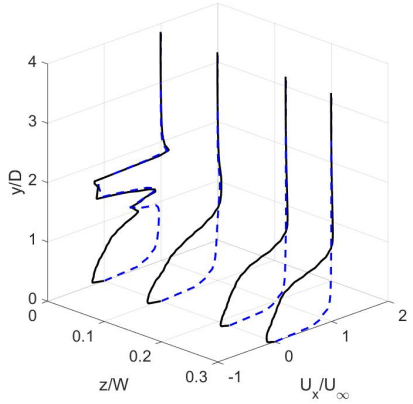

(d) $x/L = 0.26$

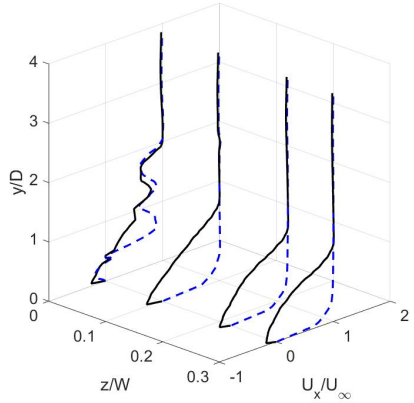

(e) $x/L = 0.34$

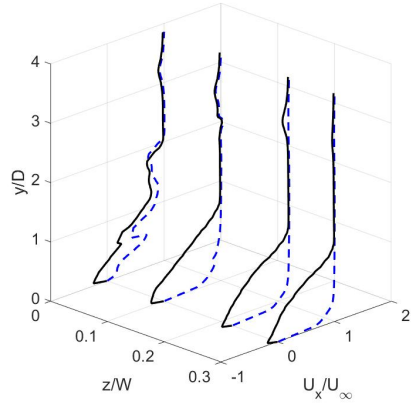

(f) $x/L = 0.43$

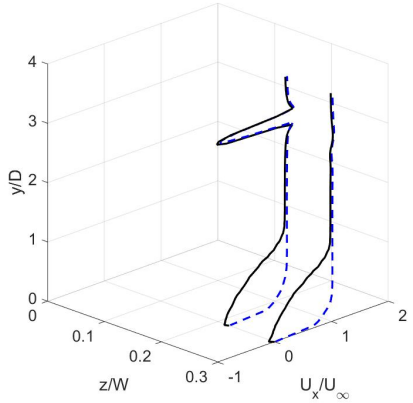

(g) $x/L = 0.45$

Figure 11: Streamwise time-averaged velocity U_x from cases 1 and 3.

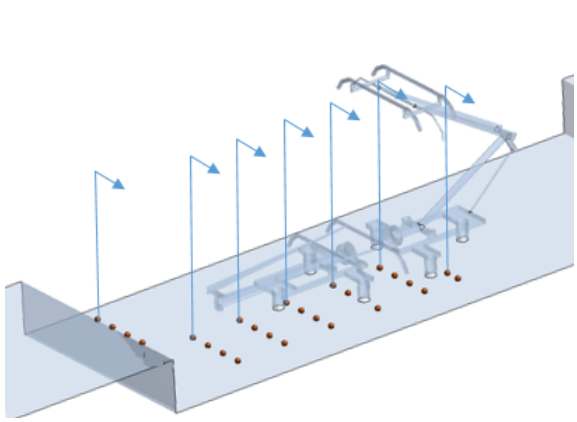

(a) Line positions

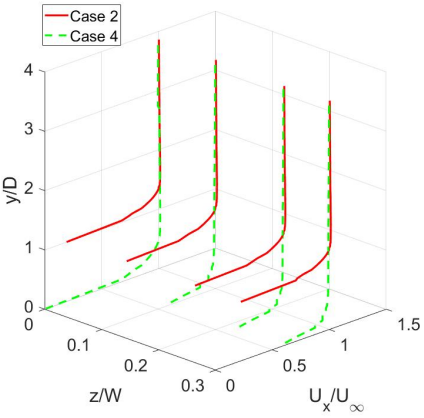

(b) $x/L = 0$

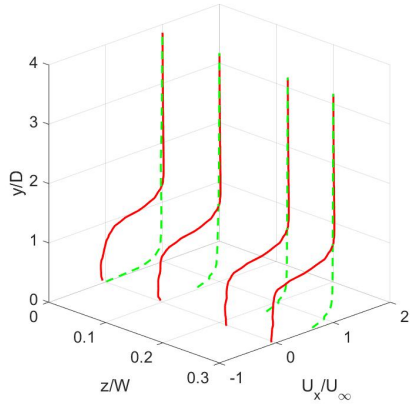

(c) $x/L = 0.17$

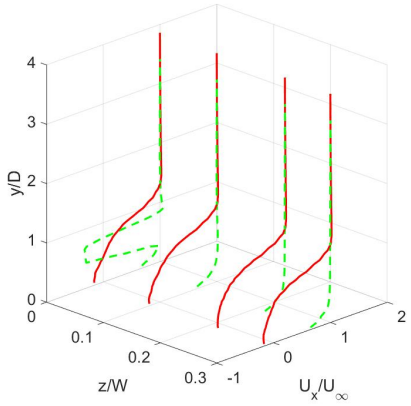

(d) $x/L = 0.26$

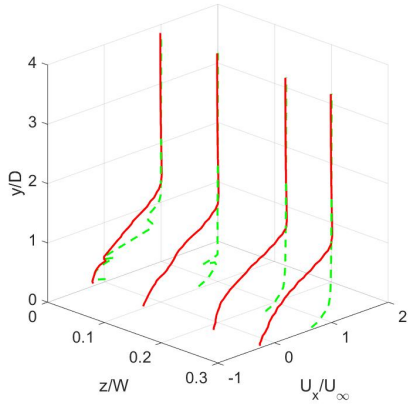

(e) $x/L = 0.34$

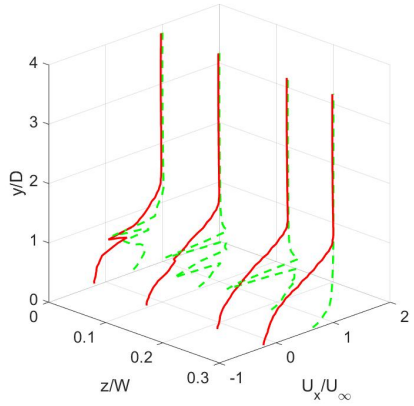

(f) $x/L = 0.43$

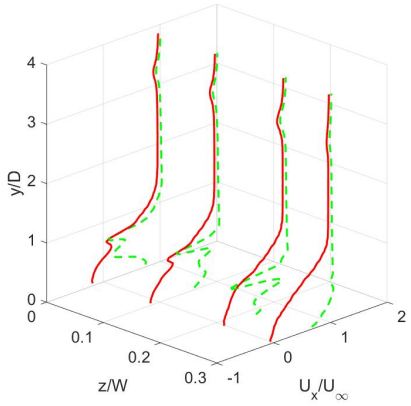

(g) $x/L = 0.52$

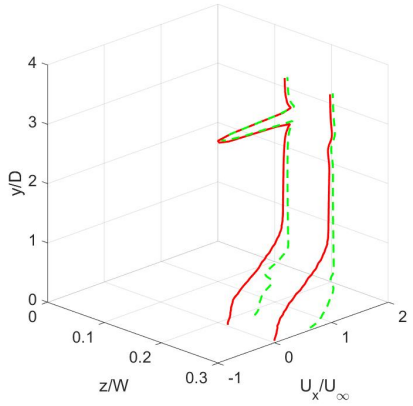

(h) $x/L = 0.54$

Figure 12: Streamwise time-averaged velocity U_x from cases 2 and 4.

5.3. RMS surface pressure

To help identify the main acoustic source regions, the wall pressure fluctuations on the pantographs are shown in Figures 13 (side view) and 14 (top view). These are shown as sound pressure levels in decibels $L_p = 10\log_{10}(\mathrm{p}^2_{\mathrm{rms}}/\mathrm{p}^2_{\mathrm{ref}})$, where p_{rms} is the rms value of pressure fluctuation and p_{ref} is the reference sound pressure (20 μPa).

The surface pressure fluctuations are generally high on the panhead, joint and top part of the lower arm for all four cases since those parts are either exposed to the freestream flow, where the flow speed is higher, or they interact with the shear layer. The downstream contact strip and horn of the raised pantograph display higher pressure fluctuations than the upstream contact strip for all cases [40], as shown in Figure 14. This is due to the shed vortices from the upstream contact strip impinging on the surface of the downstream one and the horn.

Comparing cases 1 and 2, the wall pressure on the lower arm and the control strut in case 1 has stronger fluctuations than in case 2 due to the impingement of the shear layer from the cavity leading edge. However, the surface pressure fluctuations on the joint in case 2 are higher than in case 1. This can also be found in a comparison between cases 3 and 4 since the highly unsteady flow generated from the upper part of the lower arms impinges on the joint surface. For cases 1 and 2, the rms pressure amplitude on the top surface of the panhead, frame and arm of the folded pantograph is higher than on their side surfaces. This location is where the shear layer from the cavity leading edge impinges on the top surfaces. A large pressure fluctuation appears on the downstream contact strip of the folded pantograph for cases 3 and 4, see Figure 14 (c) and (d). Compared with the contact strip of the pantograph, the surface pressure fluctuations in these areas are much higher. The folded pantograph for cases 3 and 4 is exposed to higher speed flow compared with cases 1 and 2, and therefore highly unsteady flow is generated from the upstream contact strip. This strong flow interacts with the downstream contact strip. For the rear pantograph in cases 3 and 4, there are large differences on the frame and foot regions where the pressure fluctuations are higher than for cases 1 and 2, as shown in Figure 13. This is due to the fact that a strong wake from the front pantograph frame and foot impacts on the rear one for cases 3 and 4, whereas the wake for cases 1 and 2 is weakened by the cavity.

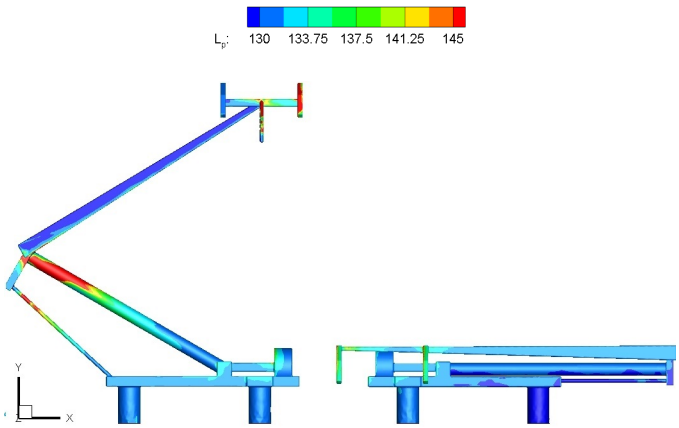

(a) Case 1

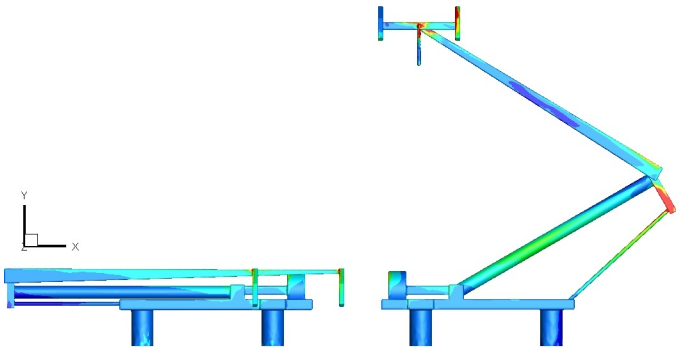

(b) Case 2

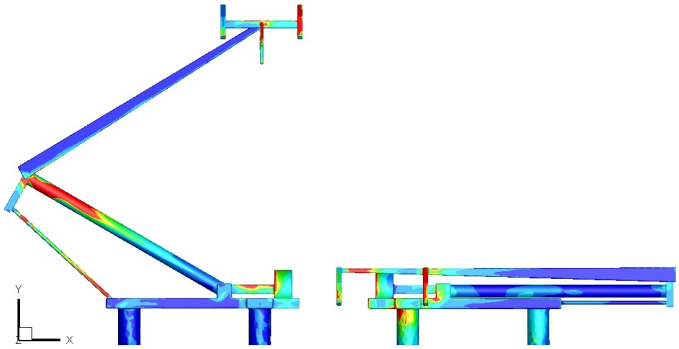

(c) Case 3

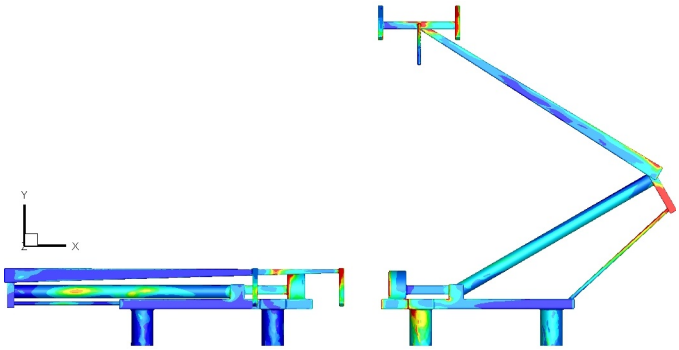

(d) Case 4

Figure 13: RMS surface pressure in decibels re 2×10^{-5} Pa

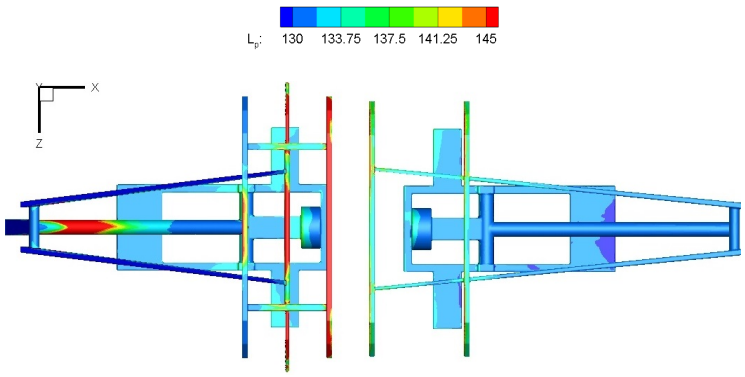

(a) Case 1

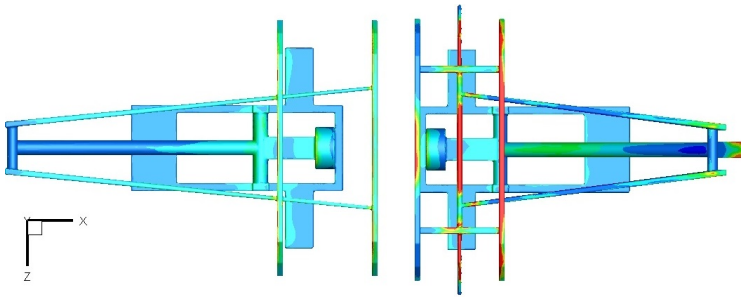

(b) Case 2

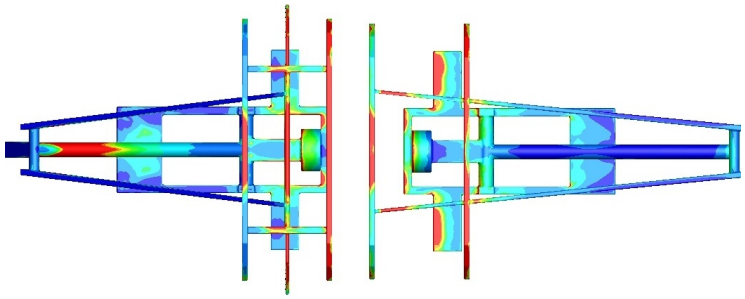

(c) Case 3

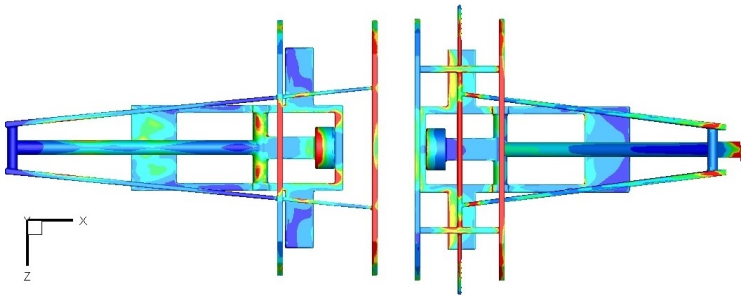

(d) Case 4

Figure 14: RMS surface pressure in decibels re 2×10^{-5} Pa

6. Aeroacoustic results

To calculate the far-field noise, the Ffowcs Williams-Hawkings (FW-H) solver was used with the integration surface for the solver coinciding with the solid walls. The unsteady pressure data on the surface of the pantographs, the cavity and the train roof are used as the input. Thus, only the contributions from dipole sources are included, whereas the contributions from quadrupole sources in the wake are neglected. This is reasonable as the contribution from quadrupole sources is small at low Mach number. The convective effects are also neglected. Far-field narrowband sound pressure spectra obtained from the simulation are converted to 1/3 octave bands and then adjusted to give the equivalent results at full scale.

6.1. Comparison between experimental and numerical results

The calculated far-field sound pressure spectra are compared with measurements from a wind tunnel for a full scale DSA350 pantograph [16]. Here, the far-field pressure radiated from a raised pantograph installed on a flat-wall is used, as the measurement was performed with only the raised pantograph. For the purpose of a mesh dependence study for the raised pantograph, coarse, medium and fine meshes are generated with 38 refinement regions, different mesh size and densities as listed in Table 5 and shown in Figure 15.

Table 5: The refinement zones and minimum cell size for each zone on pantograph (fine mesh).

Refinement region	Number of zones	Coarse	Medium	Fine
Panhead wake	4	1.5 mm	0.8 mm	0.6 mm
Upper arm wake	2	1.5 mm	1.0 mm	0.8 mm
Joint wake	1	1.5 mm	1.0 mm	0.8 mm
Lower arm wake	1	1.8 mm	1.0 mm	0.8 mm
Components	30	1.0 mm	0.4 mm	0.25mm
Total number of cells		16 million	24 million	49 million

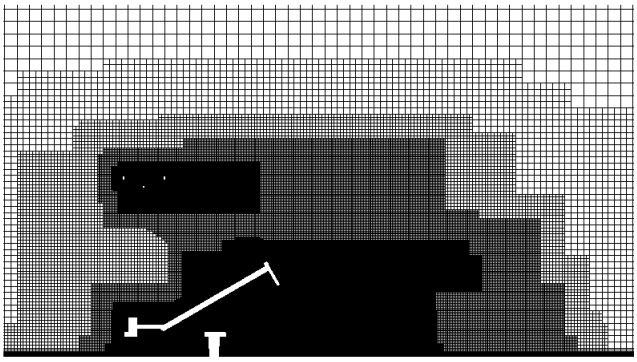

Figure 15: Overview of the mesh of the pantograph.

The microphone was located at 5 m (full scale) from the centre of the panhead at a position normal to the flow direction. The sampling frequency was 125 kHz at 1/10 scale. The spectra are obtained by segmental average using a Hanning window with 50% overlap [42]. To convert from the 1/10 scale, used for the current numerical simulations, to full scale the following aeroacoustics similarity law is used [43]:

$$L(f) = L_m(f_m) + 10\log\left(\frac{r_m D}{r D_m}\right)^2 + 10\log\left(\frac{U_\infty}{U_{\infty,m}}\right)^n \tag{7}$$

where f is the frequency, $L(f)$ is sound pressure level at frequency f, D is a characteristic length of the model, r is the distance between the sound source and the observer, U_∞ is the flow speed (83.3 m/s for the current numerical results and 97.1 m/s for the experimental test) and n is the speed exponent of the sound power, which is taken as 5.8 for the current case [18]. The values with subscript m represent values for the scale model.

Most of the cylindrical struts of the pantograph are in the sub-critical flow regime, except the lower arm of the raised pantograph. The Reynolds number of the lower arm may be in the critical flow regime ($1.4 \times 10^5 < Re \leqslant 1.0 \times 10^6$) as it has the largest diameter (D = 0.12 m for full scale). However, the lower parts of the raised pantograph for cases 1 and 2 are located in the cavity and for cases 3 and 4, the lower arm is located in the wake region of the control strut and folded pantograph respectively. Therefore, the incoming flow velocity for the lower arm in all cases is lower than the freestream velocity. Therefore, the Reynolds numbers of all components of the current pantographs are in the upper subcritical regimes ($Re \leqslant 1.4 \times 10^5$). The Strouhal number is relatively constant for a range of $10^3 < Re < 2 \times 10^5$ [43]. Hence, the full-scale frequency f can be obtained from the following equation:

$$St = \frac{fD}{U_\infty} = \frac{f_m D_m}{U_{\infty,m}} \tag{8}$$

Figure 16 shows a comparison between numerical and experimental far-field spectra in 1/3 octave bands. Although numerical results are slightly higher than measurement data in the low frequency region, excellent agreement is seen up to 800 Hz and in particular the first peak at 315 Hz, produced by the contact strips, and the second peak at 630 Hz, generated by the horns, are in good agreement with experimental data. However, because the pantograph geometry in the numerical study has been simplified by removing smaller components such as straps and springs, which generate the high frequency peaks, the numerical results do not match the measurements at high frequencies.

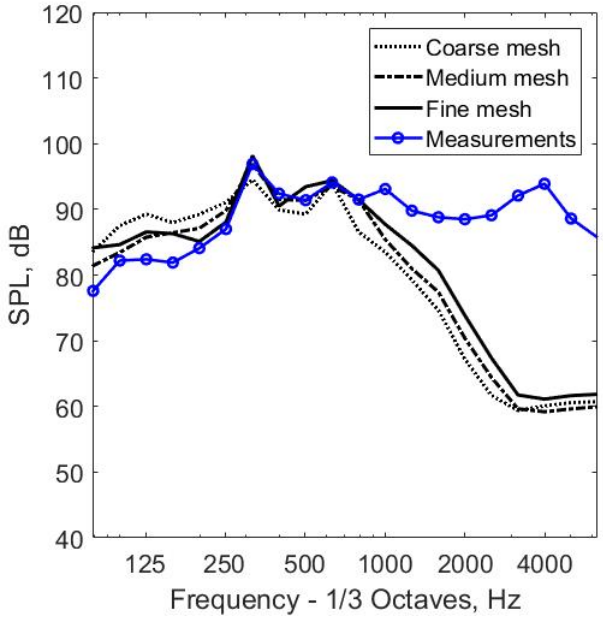

Figure 16: Sound pressure level comparison of experimental [18] and numerical results.

6.2. Sound pressure level

A total of 244 far-field receivers are used in the model, located on a sphere with radius 2.5 m (corresponding to a radius of 25 m at full scale) from the middle of the cavity floor. These receivers are uniformly distributed with an interval of 4.5 degrees in both circumferential and azimuthal directions. The same receiver positions are used for all four cases. The results in this section focus on the sound pressure level (SPL) at two receiver positions, at the side (an azimuthal angle $\theta = 90°$) and the top (a polar angle $\phi = 90°$). All current results are converted to full-scale level and flow speed is kept as 83.3 m/s. Figure 17 shows the spectra at the side receiver of the radiated sound pressure from all components including the cavity and both pantographs (a), the raised pantograph (b), the folded pantograph (c), and only the cavity (d).

The differences between the noise radiated when the raised pantograph is in front (cases 1 and 3) and behind (cases 2 and 4) are not significant. The noise levels with the raised pantograph in front(knee-upstream) are around 1.5 dB higher than the levels with the raised pantograph in back (knee-downstream). The total SPL for cases 3 and 4 is higher in most of the frequency range than for cases 1, 2 (with cavity). In Figure 17 (b), the noise from the raised pantograph is similar to the total noise for frequencies above 250 Hz. Two peaks are seen at 315 Hz and 630 Hz for the raised pantograph. Similar to Figure 16, these are produced by the upstream contact strip and the horn (H3 see Figure 4) respectively. The panhead is the most significant source of noise compared with other components. The amplitude of the first peak, associated with the contact strips, is highest for case 3 and lowest for case 2. This may

be related to the reduced incoming flow velocity in the vicinity of the panhead due to the cavity flow.

Figure 17 (c) shows the spectra of noise radiated from the folded pantograph. In each case, there are no strong tonal components. Furthermore, for cases 1 and 2 the folded pantograph is located in the cavity, where the flow velocity is significant lower and consequently the spectra of radiated noise are around 10 dB lower than for cases 3 and 4. The noise levels of the folded pantograph are similar for cases 3 and 4, although in the low frequency region up to 300 Hz, the level for case 3 with the folded pantograph downstream is slightly higher. This may be due to the highly unsteady flow from the frame impinging on feet of the front pantograph and the rear folded pantograph.

Figure 17 (d) shows the spectra of noise radiated from the cavity including the cavity wall and cavity aft wall for cases 1 and 2, and for comparison the empty cavity case. The tendency in all three cases is similar but in the high frequency region above 500 Hz the SPL for cases 1 and 2 is approximately 5 dB higher than for the empty cavity. Suggesting that the flow on the cavity trailing edge may be perturbed by the presence of the pantograph inside cavity. The noise radiated from the cavity is much lower than the other components, especially the raised pantograph, expect at low frequencies.

Figure 18 shows the corresponding spectra of radiated sound pressure at the top receiver position. In general, the sound pressure level at this location is much higher than that at the side location, especially for the sound radiated by the cavity. A third tonal peak at 800 Hz is observed in the spectra of the raised pantograph (Figure 18 (b)) which is radiated by the horn bush. In Figure 18 (d), it can be seen that the noise from the cavity for cases 1 and 2 is 10 dB higher than for the empty cavity in the frequency region between 200 Hz and 800 Hz. This suggests that flow downstream of the pantographs interacts with the cavity flow in the downstream region. This produces more unsteady flow and fluctuating pressure on the aft wall surface of the cavity which radiates to the top receiver. Due to the interaction between pantograph and cavity flow, radiated noise from the cavity is reduced at the side, but increased at the top. This is because the main noise source location of the cavity for the side receiver is the cavity downstream wall, whereas the cavity aft wall is the main noise source for the receiver at the top.

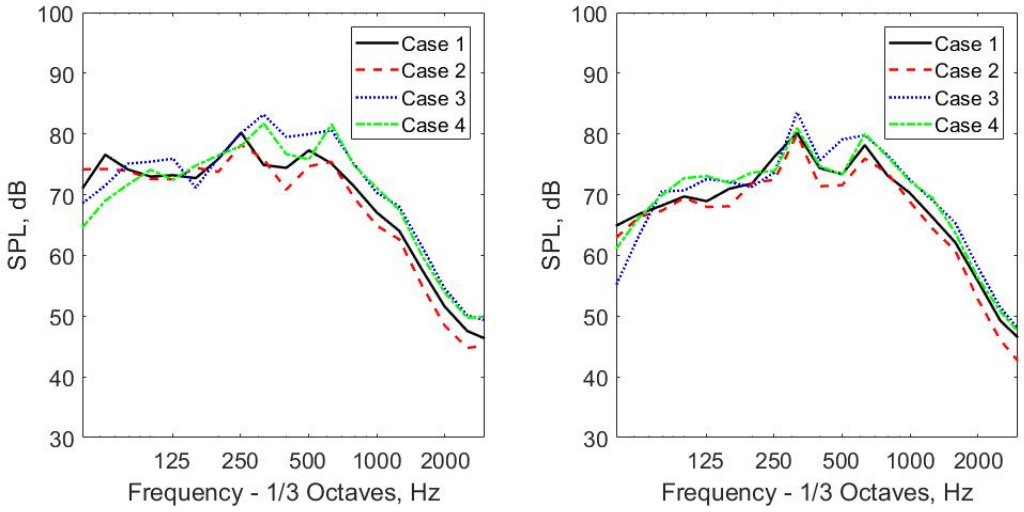

(a) Total

(b) Raised pantograph

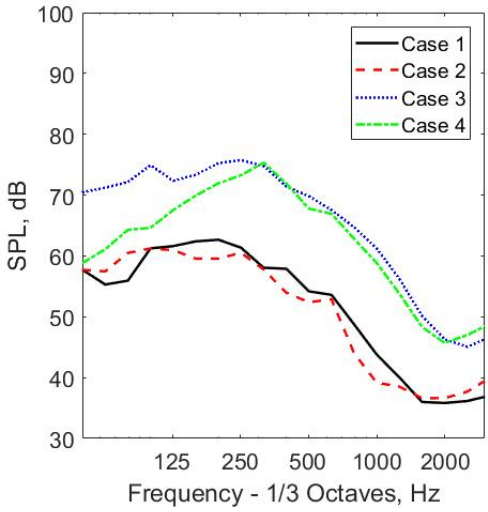

(c) Folded pantograph

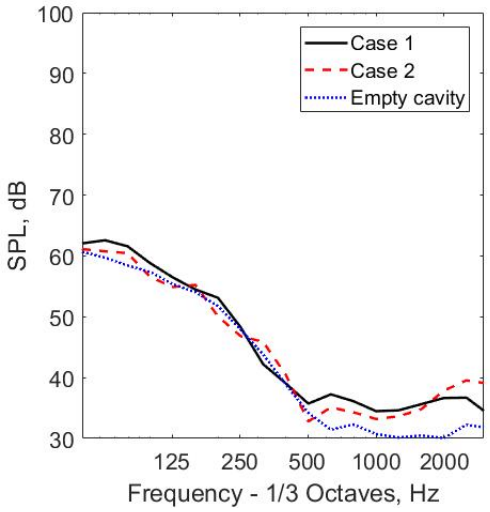

(d) Only cavity and empty cavity

Figure 17: Sound pressure levels at side receiver position.

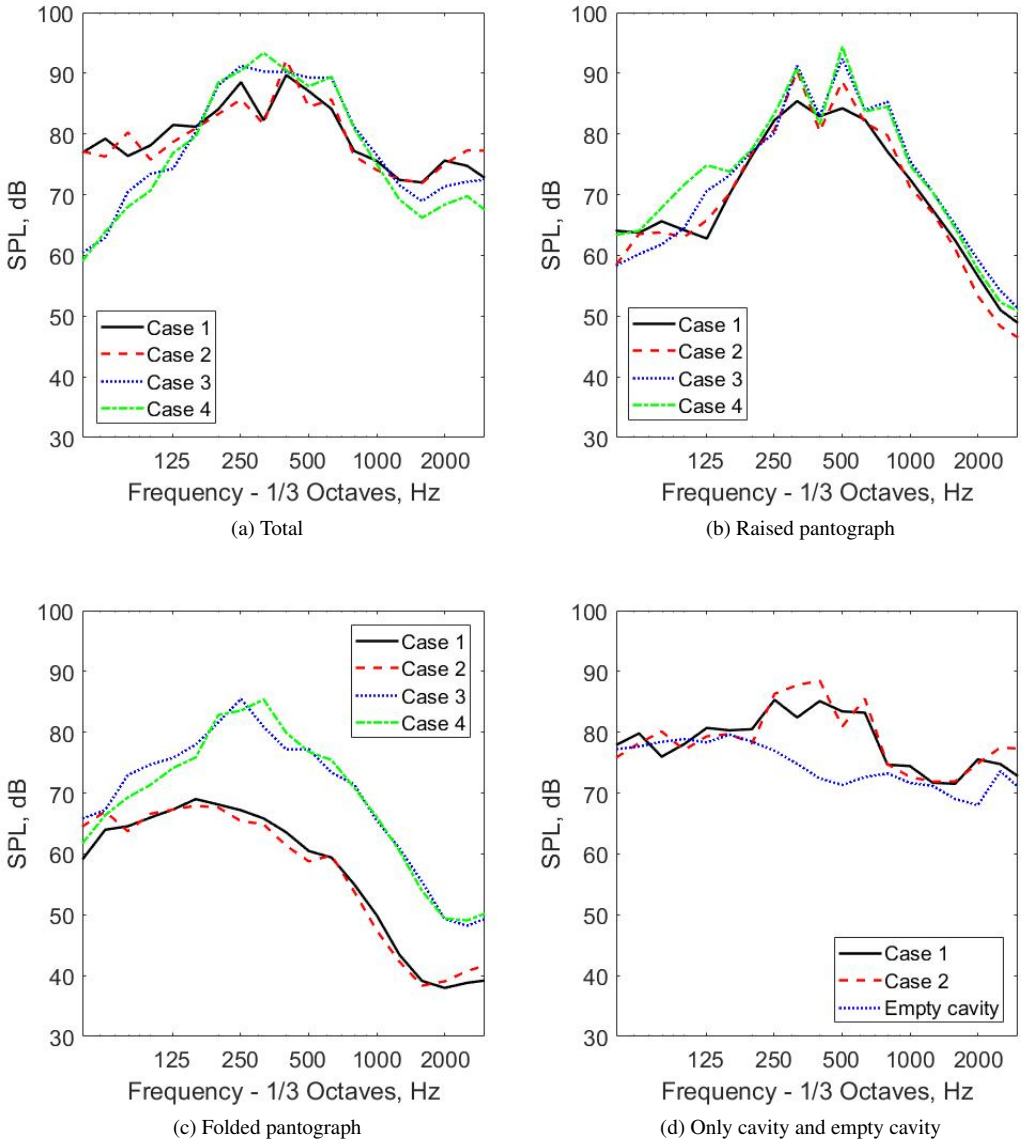

(a) Total

(b) Raised pantograph

(c) Folded pantograph

(d) Only cavity and empty cavity

Figure 18: Sound pressure levels at top receiver position.

6.3. Acoustic directivity

6.3.1. Three-dimensional directivity

Figure 19 shows the three-dimensional directivities for all cases. The overall sound pressure level (OASPL) is obtained by integrating the mean-square pressure over the frequency range up to 2500 Hz. To consider reflections from the train roof, receivers are also placed symmetrically below the cavity wall (or ground for cases 3 and 4), and the direct and reflected sound spectra are added accounting for their phase; the latter is taken from the direct radiated sound to the mirrored receiver. The OASPL is much

higher above the pantograph than to the sides for all cases. Directly above the centre of the cavity floor the level is approximately 10 dB higher than that at the side position at $\theta = 90^\circ$ for all cases. The levels downstream of the pantographs are generally greater than those in the upstream region even though convection effects are neglected.

The sound power is obtained for all cases by integrating over the full receiver grid:

$$W = \int_S \frac{p_{rms}^2}{\rho c} dS \tag{9}$$

where p_{rms} is the rms acoustic pressure, ρ is the density, c is sound speed and S is the surface area. The sound power levels are listed in Table 6. The sound powers for cases 1 and 2 are approximately 2 dB lower than for cases 3 and 4 due to the influence of the cavity flow as discussed in section 5.1.

Table 6: Sound power levels.

Simulation cases	Sound power level (dB re 10^{-12} W)	Sound power level (dBA re 10^{-12} W)
Case 0	106.5	91.8
Case 1	110.8	105.5
Case 2	111.0	105.2
Case 3	112.7	107.9
Case 4	112.8	107.8

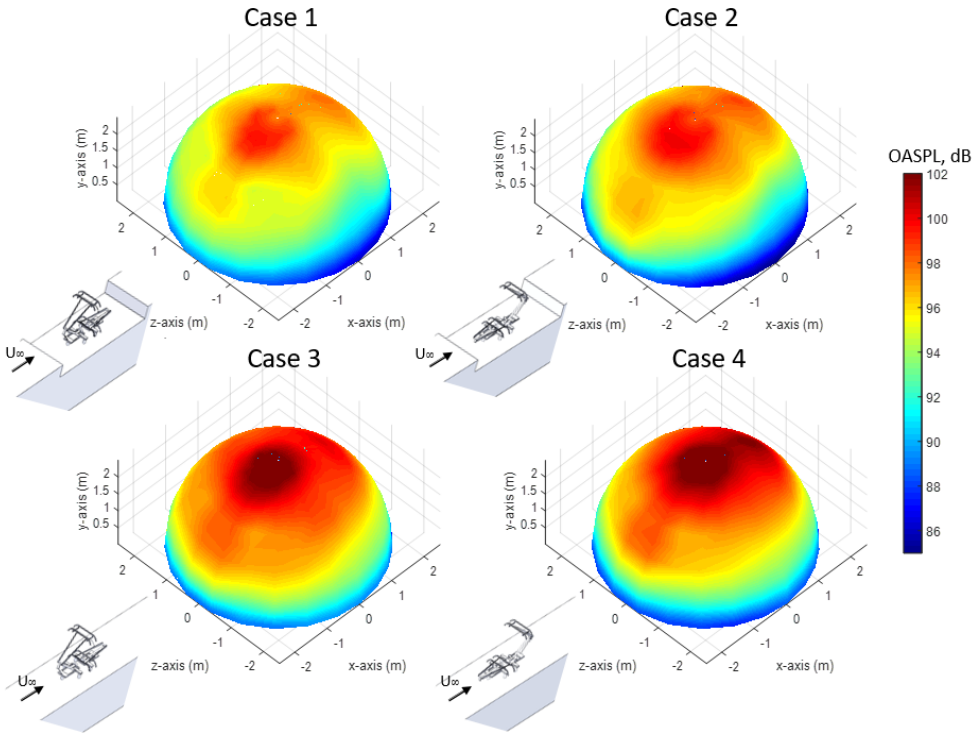

(a) Front part of isometric view

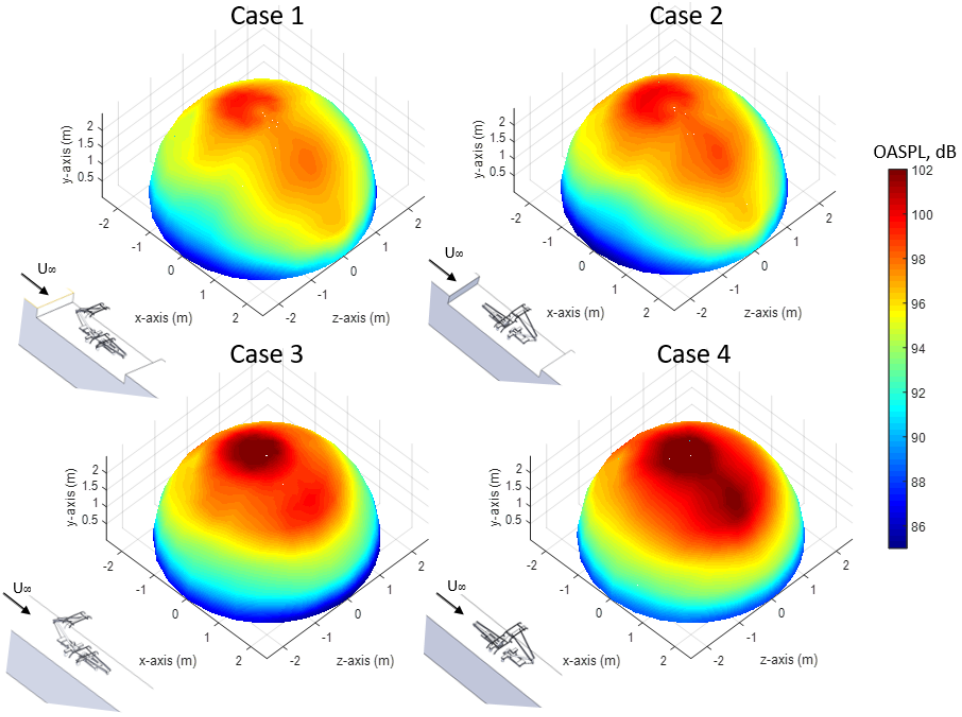

(b) Back part of isometric view

Figure 19: Three-dimensional noise directivity.

6.3.2. Side directivity

Figure 20 shows far-field directivities in a horizontal plane for the noise radiated from the whole system (a), the raised pantograph (b), the folded one (c) and the cavity (d). The directivity patterns for the noise radiated from the whole system are similar for all four cases. However, the maximum OASPL appears at $\theta = 180^\circ$ for cases 1 and 2 and at $\theta = 90^\circ$ for cases 3 and 4. The noise at $\theta = 90^\circ$ has the highest level for case 3 at 89.4 dB and for case 4, it is similar at 89.0 dB. For case 2 at the same location, the level is lower at 85.1 dB. This is because the noise level of the raised and folded pantographs for cases 1 and 2 is reduced by the cavity flow, which causes lower incoming velocity at the pantographs, as discussed in section 5.1. This can also be seen in Figure 20 (b) and (c). At $\theta = 90^\circ$, the noise level from the raised pantograph for case 3 is approximately 4 dB greater than for case 2. For the folded pantograph, there are large differences between the cases with and without the cavity; the noise level for case 3 is about 13 dB higher than that for case 2 at $\theta = 90^\circ$. The noise radiated from the cavity is not significant compared with the pantographs at the lateral position. However, its levels are still quite large at $\theta = 180^\circ$ and $\theta = 360^\circ$.

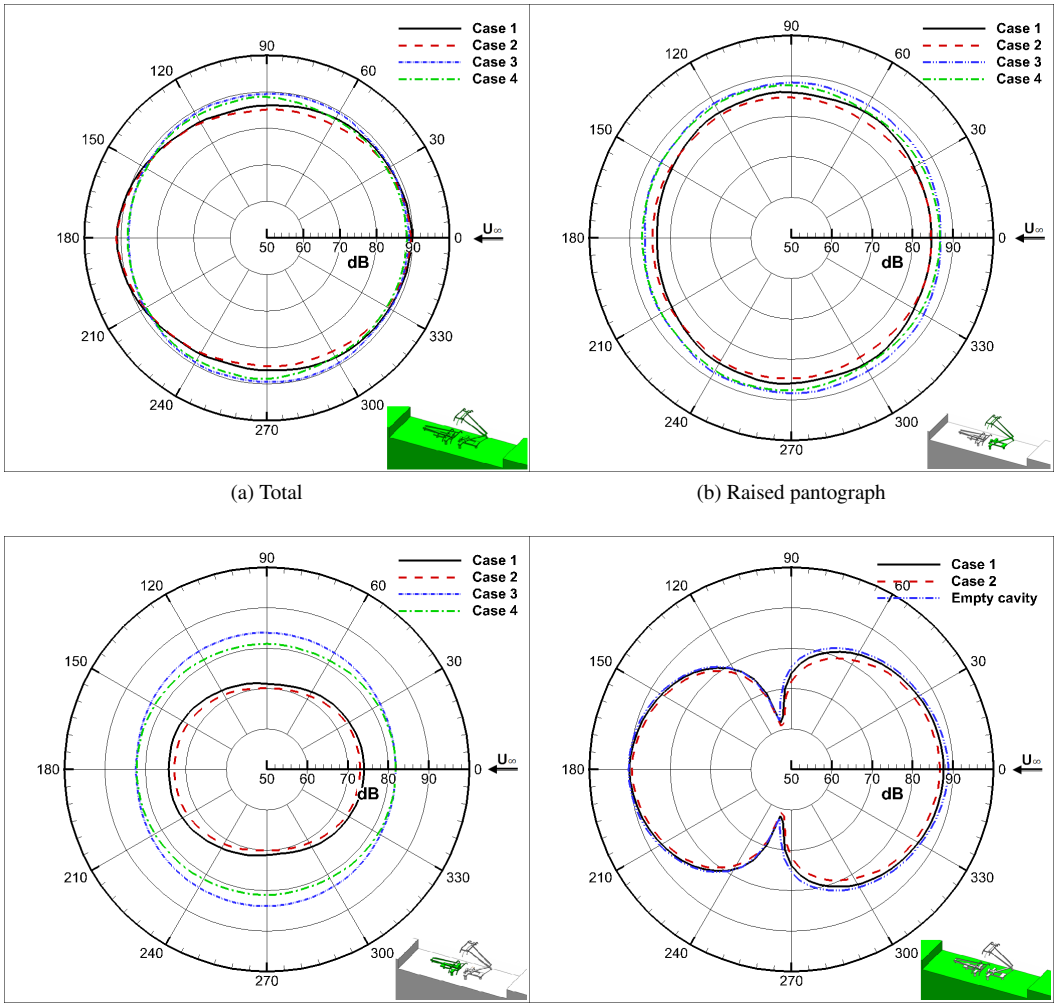

(a) Total

(b) Raised pantograph

(c) Folded pantograph

(d) Only cavity and empty cavity

Figure 20: OASPL side directivity.

7. Conclusions

To investigate the effect of the pantograph recess on its noise radiation, the flow field and radiated noise of two DSA 350 pantographs (one raised and one retracted) located in a cavity have been compared with those for the same pantographs installed on a flat train roof without the cavity. The IDDES method is used for near-field aerodynamic calculations and FW-H analogy for far-field acoustic predictions. The numerical results from the current methodology are compared with experimental data [39] in terms of the time-averaged pressure distributions of the cavity floor. The results are in good agreement with the published measurement data [39]. For far-field noise prediction, the numerical results of the raised pantograph are also in good agreement with experiment data [16] for frequency below 1 kHz.

Highly unsteady flow is present in the region of the cavity and the panhead of the raised pantograph. The separated shear layer from the cavity leading edge impinges on the pantographs and the cavity. This rolls up and becomes a spanwise vortical structure. The numerical flow visualisation shows interaction between the cavity shear layer and the pantograph. The flow separates again at the cavity trailing edge. Strong vortices are seen to be generated by the lower parts of the pantographs in cases without the cavity.

It is found that a slightly lower velocity occurs upstream of the panhead of the raised pantograph for cases with the cavity due to the effect of the cavity flow. Furthermore, the flow velocity inside the cavity is much lower than the freestream velocity. This leads to reduced surface pressure fluctuations on both the raised and the folded pantographs, and lower radiated noise levels. The largest pressure fluctuations occur on the contact strip and the horn of the raised pantograph and its lower arm for all cases. Furthermore, large fluctuations appear on the panhead and frame of the folded pantograph for cases without the cavity.

The radiated noise level is dominated by the panhead of the raised pantograph with strong tonal noise, whereas the noise radiated from the folded pantograph has no strong tonal component. A comparison between cases with and without the cavity shows that the noise from the pantographs is reduced by the cavity flow. The cavity itself also generates highly unsteady flow. Its contribution to the total noise is negligible at the side, whereas the contribution is significant to the radiated noise from the whole system at the top. When the folded pantograph is placed on the flat roof, the radiated noise from the folded pantograph is considerable, especially the folded pantograph in front and it is about 10 dB higher than that with the cavity at the side receiver. In general, the total radiated noise without the cavity is higher than that with the cavity. The difference in OASPL between the pantographs with and without the cavity was approximately 4 dB at the side. It is found that the overall SPL above the pantographs is much higher than that at the side. Furthermore, the different train running directions have no significant impact on the total noise radiated with differences of less than 1.5 dB in spectral levels and less than 1 dB in overall SPL.

This investigation has been shown that the 'closed' cavity configuration contributes reduction of noise from the pantograph because the speed of the incoming flow of the pantograph is reduced by the cavity. Furthermore, the cavity also generates significant noise itself above the high speed train whereas contribution of it at the train side the it can be ignored. This investigation can provides understanding of the effect of the cavity flow on the radiated noise from the cavity itself and other components inside the cavity.

Acknowledgments

This research project has been supported by the Iridis 4 and Lyceum High Performance Computing Facility at the University of Southampton.

References

[1] A. Jehanno, D. Palmer, and C. James, "High Speed Rail and Sustainability", Background Report: Methodology and Results of Carbon Footprint Analysis, International Union of Railways (UIC), Paris, Nov. 2011.

[2] D.J. Thompson, *"Railway noise and vibration: mechanisms, modelling and means of control"* , Oxford: Elsevier, 2008.

[3] C. Talotte, "Aerodynamic noise: a critical survey",*Journal of Sound and Vibration*, vol. 231, pp. 549-562, 2000.

[4] C. Talotte, P.E. Gautier, D.J. Thompson, and C. Hanson, "Identification, modelling and reduction potential of railway noise sources: a critical survey", *Journal of Sound and Vibration*, vol. 267, pp. 447-468, 2003.

[5] H. Noh, S. Choi, S. Hong, and S. Kim, "Investigation of noise sources in high-speed trains", Proceedings of the Institution of Mechanical Engineers, Part F: *Journal of Rail and Rapid Transit*, 2013.

[6] C. Baker, " The flow around high speed trains", *Journal of Wind Engineering and Industrial Aerodynamics*, 98(6-7), pp.277-298, 2010.

[7] T. Dong, X. Liang, S. Krajnovi, X. Xiong, W. Zhou, "Effects of simplifying train bogies on surrounding flow and aerodynamic forces", *Journal of Wind Engineering and Industrial Aerodynamics*, 191, pp. 170-182, 2019.

[8] G. Gao, F. Li, K. He, J. Wang, J. Zhang, X. Miao, "Investigation of bogie positions on the aerodynamic drag and near wake structure of a high-speed train", *Journal of Wind Engineering and Industrial Aerodynamics*, 185, pp. 41-53, 2019.

[9] J. Zhang, J. Wang, Q. Wang, X. Xiong, G. Gao, "A study of the influence of bogie cut outs' angles on the aerodynamic performance of a high-speed train", *Journal of Wind Engineering and Industrial Aerodynamics*, 175, pp. 153-168, 2018.

[10] S. Lei, Z. Chengchun, W. Jing and R. Luquan, "Numerical analysis of aerodynamic noise of a high-speed pantograph", in *Digital Manufacturing and Automation (ICDMA), 2013 Fourth International Conference on*, pp. 837-841, 2013.

[11] M. Ikeda, T. Mitsumoji, T. Sueki, and T. Takaishi, "Aerodynamic noise reduction in pantographs by shape-smoothing of the panhead and its support and by use of porous material in surface coverings", Quarterly Report of RTRI, vol. 51, pp. 220-226, 2010.

[12] M. Ikeda and T. Mitsumoji, ”Numerical estimation of aerodynamic interference between panhead and articulated frame”, Quarterly Report of RTRI, vol. 50, pp. 227-232, 2009.

[13] M. Ikeda and T. Mitsumoji, ”Evaluation method of low-frequency aeroacoustic noise source structure generated by Shinkansen pantograph”, Quarterly Report of RTRI, vol. 49, pp. 184-190, 2008.

[14] X. Liu, ”Aerodynamic noise from components of a train pantograph and its reduction,” Ph.D. Thesis, Faculty of Eng. and Environ., Univ. of Southampton., Southampton, 2017.

[15] F.R. Grosche and G. Meier, ”Research at DLR Göttingen on bluff body aerodynamics, drag reduction by wake ventilation and active flow control”, *Journal of Wind Engineering and Industrial Aerodynamics*, vol. 89, pp. 1201-1218, 2001.

[16] T. Lölgen, ”Wind tunnel noise measurements on full-scale pantograph models”, *The Journal of the Acoustical Society of America*, 105(2) 1136. doi: 10.1121/1.425410, 1999.

[17] H.H. Yu J.C. Li, and H.Q. Zhang, ”On aerodynamic noises radiated by the pantograph system of high-speed trains”, *Acta Mechanica Sinica*, vol. 29, pp. 399-410, 2013.

[18] E.Latorre. Iglesias, D.J. Thompson, M.G Smith, ”Component-based model to predict aerodynamic noise from high-speed train pantographs”, *Journal of Sound and Vibration*, 394, pp.280-305, 2017.

[19] C. Noger, J.C. Patrat, J. Peube, J.L. Peube ”Aeroacoustical study of the TGV pantograph recess”, *Journal of Sound and Vibration*, 231 (3), pp. 563-575, 2000.

[20] M. Carnevale, A. Facchinetti, L. Maggiori, D. Rocchi ”Computational fluid dynamics as a means of assessing the influence of aerodynamic forces on the mean contact force acting on a pantograph”, *Proceedings of the Institution of Mechanical Engineers, Part F: Journal of Rail and Rapid Transit*, 230(7), pp.1698-1713, 2016

[21] L. Jia, D. Zhou, J. Niu, ”Numerical calculation of boundary layers and wake characteristics of high-speed trains with different lengths”, *PloS one*, 12(12), e0189798, 2017.

[22] J.D Anderson Jr, *”Fundamentals of aerodynamics,”*, New York: McGraw-Hill Education, 2010.

[23] P. R. Spalart, ”Comments on the feasibility of LES for wings, and on a hybrid RANS/LES approach,”*Proceedings of first AFOSR international conference on DNS/LES*, Greyden Press, 1997.

[24] ANSYS, ”ANSYS Fluent Tutorial Guide,” ANSYS, Inc. Canonsburg, PA, 2014.

[25] P. R. Spalart, S. Deck, M. L. Shur, K. D. Squires,M. K. Strelets and A. Travin, ”A new version of detached-eddy simulation, resistant to ambiguous grid densities,” *Theoretical and computational fluid dynamics*, vol. 20(3), pp.181-195. 2006

[26] P. R. Spalart, ”Strategies for turbulence modelling and simulations,” *International Journal of Heat and Fluid Flow*, vol. 21, pp. 252-263, 2000.

[27] M. L. Shur, P. R. Spalart, M.K. Strelets, A.K. Travin, ”A hybrid RANS-LES approach with delayed-DES and wall-modelled LES capabilities,” *23rd AIAA/CEAS Aeroacoustics Conference*, vol. 28(6), pp. 1638-1649, 2008.

[28] M. J. Lighthill, ”On sound generated aerodynamically. I. General theory,” in *Proceedings of the Royal Society of London A: Mathematical, Physical and Engineering Sciences*, pp. 564-587, 1952.

[29] A. P. Dowling and J. F. Williams, ”Sound and sources of sound,” Ellis Horwood Ltd., Chichester: J. Wiley and Sons, 1983.

[30] J. F. Williams and D. L. Hawkings, ”Sound generation by turbulence and surfaces in arbitrary motion,” *Philosophical Transactions of the Royal Society of London A: Mathematical*, Physical and Engineering Sciences, vol. 264, pp. 321-342, 1969.

[31] Hövelmann, Andreas. ”Aerodynamic investigations of noise-reducing high-lift systems for passenger transport aircraft,” Diploma Thesis, Dept. of Aeronautical and Vehicle Eng., Royal Inst. of Techno., Stockholm, 2011.

[32] D. P. Lockard, M. M. Choudhari, M. D. OConnell, B. M. Duda, E. Fares, ”Noise Simulations of the High-Lift Common Research Model,” *23rd AIAA/CEAS Aeroacoustics Conference*, pp. 3362, 2017.

[33] L. Wen, ”Numerical Investigation of Landing Gear Noise,” Ph.D. Thesis, Faculty of Eng. and Environ., Univ. of Southampton., Southampton, 2011.

[34] P. R. Spalart, M. L. Shur, M. K.Strelets, A. K. Travin, ”Towards noise prediction for rudimentary landing gear,” *Procedia IUTAM*, pp.283-292, 2010.

[35] N. Paradot, E. Masson, F. Poisson, R. Grgoire, E. Guilloteau, H. Touil, P. Sagaut, Paradot, N., E. Masson, F. Poisson, R. Grgoire, E. Guilloteau, H. Touil, and P. Sagaut. ”Aero-acoustic methods for high-speed train noise prediction,” *Proceedings of the World Congress in Railway Research (WCRR)*, Seoul, Korea, 2008

[36] J. Y. Zhu, Z. W. Hu, D. J. Thompson, "The flow and flow-induced noise behaviour of a simplified high-speed train bogie in the cavity with and without a fairing," *Proceedings of the Institution of Mechanical Engineers, Part F: Journal of Rail and Rapid Transit*, 232(3), pp.759-773, 2018

[37] K. S. Brentner and F. Farassat, "An analytical comparison of the acoustic analogy and Kirchhoff formulation for moving surfaces," *The American Helicopter Society 53rd Annual Forum*, Virginia Beach, VA, May 1, 1997.

[38] K. S. Brentner and F. Farassat, "Modeling aerodynamically generated sound of helicopter rotors," *Progress in Aerospace Sciences*, vol. 39, pp. 83-120, 2003.

[39] E. B. Plentovich, R.L. Stallings, and M.B. Tracy, "Experimental cavity pressure measurements at subsonic and transonic speeds. Static-pressure results," NASA Langley Res. Cent., Hampton, VA, Tech. paper TP-3358, 1993.

[40] M. Carnevale, A. Facchinetti, and D. Rocchi, "Assessing aerodynamic effects on a railway pantograph by means of computational fluid dynamics", *In Railways 2016-The Third International Conference on Railway Technology: Research, Development and Maintenance*, pp. 1-15, 2016..

[41] M. M. Zdravkovich, "Flow Around Circular Cylinders, vol. 2. Application s," Oxford University Press, 2003.

[42] Z. Hu, C.L. Morfey, and N.D. Sandham, "Wall pressure and shear stress spectra from direct simulations of channel flow," *AIAA journal*, vol 44(7), pp.1541-1549, 2006.

[43] A. Iida, T. Otaguro, H. Nagarekawa, A. Torii, and I. Naruse, "Similarity law of aerodynamic noise generation," in *6th AIAA Aeroacoustics Conference and Exhibit Conf.*, Lahaina., pp.2000-2012, 2000.

[44] V. Thangamni, K. Knowles, and A. J. Saddington, "Effects of Scaling on High Subsonic Cavity Flow Oscillations and control," *Journal of Aircraft.*, vol 51(2), pp.424-433, 2014.